# SPINNING RED CLOCKS IN CROWDED FIELDS

A DISSERTATION SUBMITTED TO THE GRADUATE DIVISION OF THE UNIVERSITY OF HAWAIʻI IN PARTIAL FULFILLMENT OF THE REQUIREMENTS FOR THE DEGREE OF

DOCTOR OF PHILOSOPHY

IN

ASTRONOMY

OCTOBER 2022

By
Ryan Dungee

Dissertation Committee:

M. Chun, Chairperson
J. van Saders
E. Gaidos
C. Baranec
E. Magnier
S. Businger

To all of the birds I will one day meet who will never care that I am a doctor.

# Acknowledgements

The list of people worthy of thanks for their help in completing this thesis rivals the length of it. Nonetheless, there are a few folks in particular I must thank for endless hours they have spent dealing with my madness. My cohort, Zach, Deep, and Ashley, what an incredible journey it has been and I look forward to seeing where we all go from here. Jess and Max, you two helped to make Hilo really feel like home. And finally Mark, I could not have asked for a better advisor.

# Abstract

To build a clear picture of the history of our Milky Way galaxy we need to be able to reliably measure the ages of the stars within it. Unfortunately the most common stars, M dwarfs, are resistant to most of our current age measuring techniques. This leaves gyrochronology, the use of an empirical relation between rotation and age, as our method for measuring M dwarf ages. Successful gyrochronology requires the study of open clusters spanning as wide a range of ages and metallicities as possible. In this dissertation I present the work I have done on advancing our understanding of spin-down in late K and early M dwarfs through observations of the 4 Gyr old open cluster M67. Future studies that include a wider sample of open clusters, and that push the observations to lower mass stars, will require high spatial resolution wide-field imaging to remain feasible. To this end, this dissertation also presents the work I have done in developing an advanced technique for the control systems of ground layer adaptive optics. This technique, which we have dubbed "temporal tomography" is expected to facilitate the widespread adoption of ground layer adaptive optics by reducing the number of guide stars needed to obtain accurate estimates of the ground layer turbulence. These systems will be capable of imaging crowded fields, such as the open clusters needed for calibrating gyrochronology.

# Table of Contents

# List of Tables

# List of Figures

# Chapter 1

# Introduction

## 1.1 Project Overview

In order to build a clear picture of the history of any system—be it stars, planets, or the Milky Way itself, we must understand the order in which events occur and the timescales on which they happen. This demands precise, reliable stellar ages. There are a variety of methods to achieve this, some of which are based on stellar models (e.g., isochrone fitting, Hidalgo et al. 2018, Howes et al. 2019; or asteroseismology, Creevey et al. 2017), while others are based on statistical correlations (e.g., Li abundances, Soderblom et al. 1993; or peculiar velocities, Wielen 1977). Importantly, all of these methods had to be benchmarked against open clusters before they could be applied to field stars. There is a problem though, the most common type of star in the galaxy are M dwarfs (Gould et al. 1996; Bochanski et al. 2010), and they are resistant to the majority of these stellar age-dating methods. M dwarf evolution on the main sequence is undetectable (Laughlin et al. 1997), they also have no observable asteroseismic oscillations (Chaplin et al. 2011; Berdiñas et al. 2017; Mathur et al. 2019). Moreover, their deep convective envelopes burn Li within the first  50 Myrs (Bildsten et al. 1997) and a statistical relation such as age-peculiar velocity is unreliable for individual stars, and breaks down for stars which are too young or too old (Aumer & Binney 2009; Lu et al. 2021). These issues are particularly problematic because M dwarfs are excellent probes of the galactic history of a variety of processes. This is owed to the fact

that: M dwarfs have higher occurrence rates of small planets compared to higher mass stars (Dressing & Charbonneau 2015; Hardegree-Ullman et al. 2019), they do not fuse heavy elements, and many tens of Gyr will pass before they show any signs of evolution on a Hertzsprung–Russell diagram (Laughlin et al. 1997).

Thankfully, rotation period-age relations, or *gyrochronology*, show promise for M dwarf age-dating (Barnes 2003). Gyrochronology is based on the fact that stars spin down over time as a result of the interaction between their magnetic fields and stellar winds, resulting in a loss of angular momentum over time (Weber & Davis 1967; Skumanich 1972; Barnes 2007). As with any of the other techniques, accurate gyrochronology requires calibration. Prior to my work presented in this dissertation, M dwarf spin-down was effectively uncalibrated beyond the age of 670 Myr, with just a handful of M0 stars having known ages and rotation periods. Using M67, a 4 Gyr old open cluster, we have changed this. We measured the rotation periods of stars approaching the fully convective boundary, and used their rotation periods to make a compelling case for core-envelope decoupling theory, publishing these results in the Astrophysical Journal.

While the M dwarfs of M67 have provided critical insight into the late stages of M dwarf spin-down, there is still much work to be done on intermediate ages. In particular the precise time to the resumption of M dwarf spin-down is required for careful calibration of gyrochronology, and such tests are still lacking the needed calibrators. Collecting all of the known spin-down calibrators and plotting them in age versus effective temperature highlights this, as can be seen in Fig. 1.2, where only a handful of M dwarf calibrators exist between the stars of Praesepe (still subject to initial conditions) and M67 (old enough to have resumed spin-down). This highlights a need for further observations, including both a larger sample of clusters as well as deeper observations in order to obtain later spectral types.

However, stellar clusters are by nature crowded fields and they often span tens of arcminutes on-sky. With most clusters being in the galactic plane, this can very quickly lead to observations in fields with a high degree of crowding. Ground layer adaptive optics

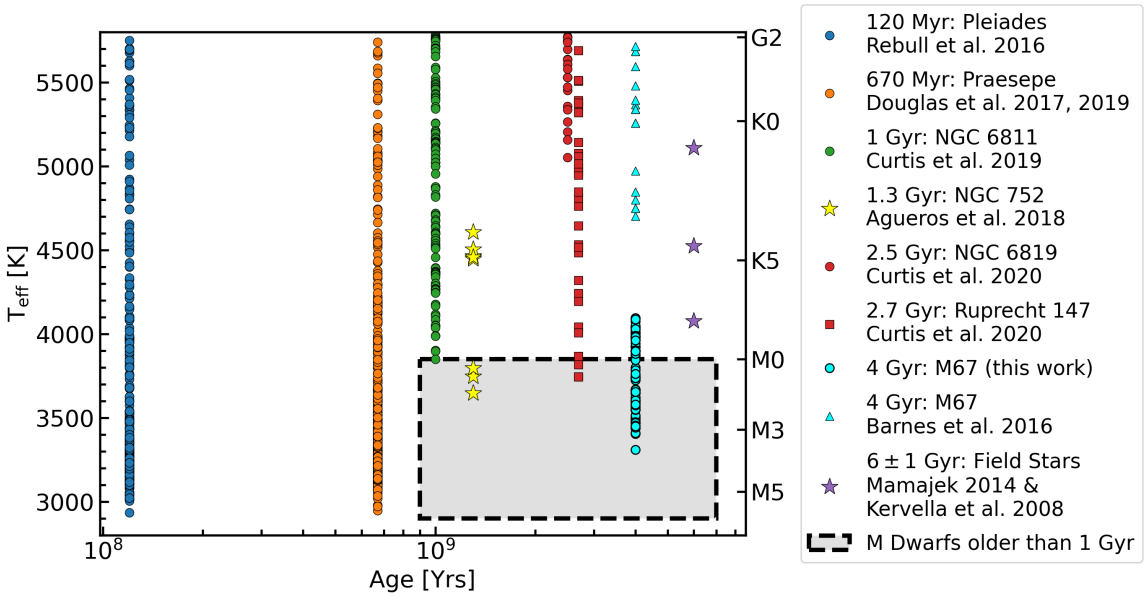


Figure 1.1: A collection of the available spin-down calibrators plotted as age versus the effective temperature. Benchmarks include the Pleiades (120 Myr; Rebull et al. 2016), Praesepe (670 Myr; Douglas et al. 2017, 2019), NGC 6811 (1 Gyr; Curtis et al. 2019), NGC 752 (1.4 Gyr; Agüeros et al. 2018), NGC 6819/Ruprecht 147 (2.5 Gyr projected forward by Curtis et al./2.7 Gyr; Meibom et al. 2015; Curtis et al. 2020), M67 (4 Gyr; Barnes et al. 2016, and this work), and three field stars: $\alpha$ Cen B and 61 Cyg A and B (Table 3 of Curtis et al. 2020, and references therein).

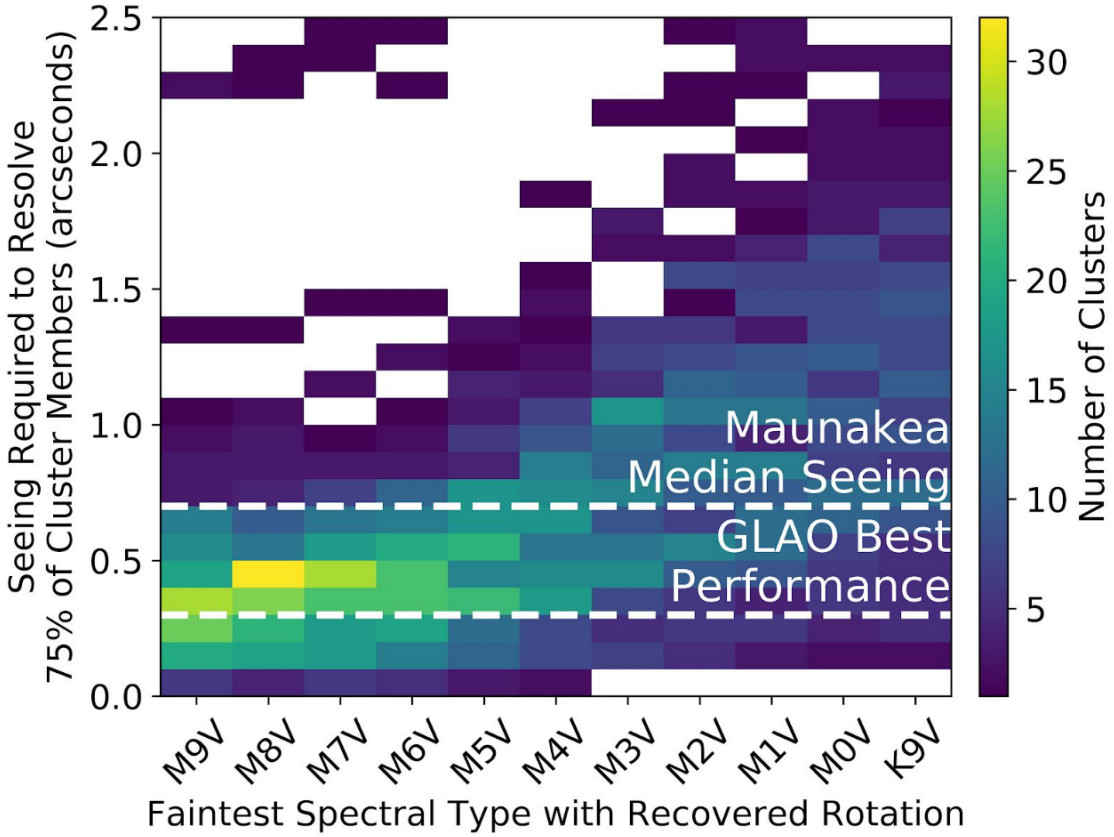


Figure 1.2: Crowding in the field of an open cluster versus the faintest spectral type with a measured rotation period. There is a clear trend that cluster become more crowded with observations for lower mass spectral types. All clusters included are at least 1 Gyr of age, and thus are suitable targets for spin-down calibration. Clusters requiring better than median seeing need ground layer or multi-conjugate adaptive optics systems in order to achieve high enough cadence in observations.

(GLAO) is especially helpful in these circumstances. It can provide a factor 2-3 improvement in spatial resolution over fields of view large enough to capture entire clusters in one pointing (Rigaut 2002). We have estimated the need for GLAO with some simple simulations. First, I assumed that cluster members are distributed using a King profile (King 1966) with profile parameters from the WEBDA[1] open cluster catalog. Field star populations were simulated with the Besançon galactic model Robin et al. (2003) distributed uniformly across the field of view. I then estimated the spatial resolution needed to sufficiently resolve individual cluster members down to a specific spectral type (Fig. 1.1) by setting the requirement that at least 75% of cluster members must be separable from their nearest neighbor, assuming a Gaussian point spread function. In doing this we see that observations of fully convective members of open clusters generally require better than median seeing values, restricting the number of nights available for observing. However, with GLAO the majority of clusters can be observed a majority of the time. Unfortunately, GLAO requires a high number of guide stars in order to effectively reconstruct the ground layer turbulence for the adaptive optics correction. For natural guide star systems, this greatly limits the number of fields where the system can achieve effective correction, and for laser guide star systems this can drive the cost of development up, preventing many smaller observatories from having a GLAO system.

In this dissertation I also present the work I have done on developing a new approach to tomography in a GLAO system. It relies on the fact that atmospheric layers with different wind velocities have unique temporal characteristics. Which, in concert with external measurements of the vertical wind profile, allows one to assign altitudes to the atmospheric layers based on their wind velocity alone. Moreover, temporally filtering the data allows one to select individual layers to correct for. Our simulations indicated that effective "temporal tomography" will allow GLAO systems to operate using fewer guide stars, facilitating a more widespread adoption of the technology. There is still work to be done before this work is published, including the development of more detailed simulations, as well as a formalized

[1]Which can be found on this website.

mathematical framework for the design of the temporal filters. Nonetheless, I have laid the important groundwork needed for developing temporal tomography. Thus, this work has both advanced the field of gyrochronology through observations of M67 and developed new techniques to aid in the creation of systems capable of pushing future calibrations to the later M dwarfs.

## 1.2 Table of Acronyms

Table 1.1: A list of all the acronyms that are used in this dissertation, in alphabetical order.

| Term | Acronym |
|---|---|
| Adaptive Optics | AO |
| Canada France Hawaii Telescope | CFHT |
| Charge-Coupled Device | CCD |
| Color–Magnitude Diagram | CMD |
| Deformable Mirror | DM |
| Differential Image Motion Monitor | DIMM |
| Discrete Fourier Transform | DFT |
| Extreme Adaptive Optics | ExAO |
| False Alarm Probability | FAP |
| Fast Fourier Transform | FFT |
| Finite Impulse Response | FIR |
| Fourier Transform Reconstruction | FTR |
| Fourier Wind Identification | FWI |
| Full-width at half-maximum | FWHM |
| Global Forecasting System | GFS |
| Ground Layer Adaptive Optics | GLAO |
| Guide Star | GS |
| Infinite Impulse Response | IIR |
| Lomb-Scargle | LS |
| Multi-Aperture Scintillation Sensor | MASS |
| Multi-Conjugate Adaptive Optics | MCAO |
| Optimized-gain Fourier Control | OFC |
| Pan-STARRS | PS1 |
| Predictive Fourier Control | PFC |
| Probability Distribution Function | PDF |
| Power Spectral Density | PSD |
| Real Time Controller | RTC |
| Renormalized Unit Weight Error | RUWE |
| Scintillation Detection and Ranging | SCIDAR |
| Slope Detection and Ranging | SLODAR |
| University of Hawaii 88" Telescope | UH88" |
| Wavefront Sensor | WFS |

# References


Agüeros, M. A., Bowsher, E. C., Bochanski, J. J., Cargile, P. A., Covey, K. R., Douglas, S. T., Kraus, A., Kundert, A., Law, N. M., Ahmadi, A., & Arce, H. G. 2018, ApJ, 862, 33

Aumer, M. & Binney, J. J. 2009, MNRAS, 397, 1286

Barnes, S. A. 2003, ApJ, 586, L145

—. 2007, ApJ, 669, 1167

Barnes, S. A., Weingrill, J., Fritzewski, D., Strassmeier, K. G., & Platais, I. 2016, ApJ, 823, 16

Berdiñas, Z. M., Rodríguez-López, C., Amado, P. J., Anglada-Escudé, G., Barnes, J. R., MacDonald, J., Zechmeister, M., & Sarmiento, L. F. 2017, MNRAS, 469, 4268

Bildsten, L., Brown, E. F., Matzner, C. D., & Ushomirsky, G. 1997, ApJ, 482, 442

Bochanski, J. J., Hawley, S. L., Covey, K. R., West, A. A., Reid, I. N., Golimowski, D. A., & Ivezić, Ž. 2010, AJ, 139, 2679

Chaplin, W. J., Bedding, T. R., Bonanno, A., Broomhall, A. M., García, R. A., Hekker, S., Huber, D., Verner, G. A., Basu, S., Elsworth, Y., Houdek, G., Mathur, S., Mosser, B., New, R., Stevens, I. R., Appourchaux, T., Karoff, C., Metcalfe, T. S., Molenda-Żakowicz, J., Monteiro, M. J. P. F. G., Thompson, M. J., Christensen-Dalsgaard, J., Gilliland,

R. L., Kawaler, S. D., Kjeldsen, H., Ballot, J., Benomar, O., Corsaro, E., Campante, T. L., Gaulme, P., Hale, S. J., Handberg, R., Jarvis, E., Régulo, C., Roxburgh, I. W., Salabert, D., Stello, D., Mullally, F., Li, J., & Wohler, W. 2011, ApJ, 732, L5

Creevey, O. L., Metcalfe, T. S., Schultheis, M., Salabert, D., Bazot, M., Thévenin, F., Mathur, S., Xu, H., & García, R. A. 2017, A&A, 601, A67

Curtis, J. L., Agüeros, M. A., Douglas, S. T., & Meibom, S. 2019, ApJ, 879, 49

Curtis, J. L., Agüeros, M. A., Matt, S. P., Covey, K. R., Douglas, S. T., Angus, R., Saar, S. H., Cody, A. M., Vanderburg, A., Law, N. M., Kraus, A. L., Latham, D. W., Baranec, C., Riddle, R., Ziegler, C., Lund, M. N., Torres, G., Meibom, S., Aguirre, V. S., & Wright, J. T. 2020, ApJ, 904, 140

Douglas, S. T., Agüeros, M. A., Covey, K. R., & Kraus, A. 2017, ApJ, 842, 83

Douglas, S. T., Curtis, J. L., Agüeros, M. A., Cargile, P. A., Brewer, J. M., Meibom, S., & Jansen, T. 2019, ApJ, 879, 100

Dressing, C. D. & Charbonneau, D. 2015, ApJ, 807, 45

Gould, A., Bahcall, J. N., & Flynn, C. 1996, ApJ, 465, 759

Hardegree-Ullman, K. K., Cushing, M. C., Muirhead, P. S., & Christiansen, J. L. 2019, AJ, 158, 75

Hidalgo, S. L., Pietrinferni, A., Cassisi, S., Salaris, M., Mucciarelli, A., Savino, A., Aparicio, A., Silva Aguirre, V., & Verma, K. 2018, ApJ, 856, 125

Howes, L. M., Lindegren, L., Feltzing, S., Church, R. P., & Bensby, T. 2019, A&A, 622, A27

King, I. R. 1966, AJ, 71, 64

Laughlin, G., Bodenheimer, P., & Adams, F. C. 1997, ApJ, 482, 420

Lu, Y. L., Angus, R., Curtis, J. L., David, T. J., & Kiman, R. 2021, AJ, 161, 189

Mathur, S., García, R. A., Bugnet, L., Santos, Â. R. G., Santiago, N., & Beck, P. G. 2019, Frontiers in Astronomy and Space Sciences, 6, 46

Meibom, S., Barnes, S. A., Platais, I., Gilliland, R. L., Latham, D. W., & Mathieu, R. D. 2015, Nature, 517, 589

Rebull, L. M., Stauffer, J. R., Bouvier, J., Cody, A. M., Hillenbrand, L. A., Soderblom, D. R., Valenti, J., Barrado, D., Bouy, H., Ciardi, D., Pinsonneault, M., Stassun, K., Micela, G., Aigrain, S., Vrba, F., Somers, G., Christiansen, J., Gillen, E., & Collier Cameron, A. 2016, AJ, 152, 113

Rigaut, F. 2002, in European Southern Observatory Conference and Workshop Proceedings, Vol. 58, European Southern Observatory Conference and Workshop Proceedings, 11

Robin, A. C., Reylé, C., Derrière, S., & Picaud, S. 2003, A&A, 409, 523

Skumanich, A. 1972, ApJ, 171, 565

Soderblom, D. R., Jones, B. F., Balachandran, S., Stauffer, J. R., Duncan, D. K., Fedele, S. B., & Hudon, J. D. 1993, AJ, 106, 1059

Weber, E. J. & Davis, Leverett, J. 1967, ApJ, 148, 217

Wielen, R. 1977, A&A, 60, 263

# Chapter 2

# A 4-Gyr M Dwarf Gyrochrone from CFHT/MegaPrime Monitoring of the Open Cluster M67

Note: This chapter originally appeared as Dungee et al. 2022 in Astrophysical Journal (ApJ), with co-authors Jennifer van Saders, Eric Gaidos, Mark Chun, Rafael A. García, Eugene A. Magnier, Savita Mathur, and Ângela R. G. Santos

## Abstract

We present stellar rotation periods for late K and early M dwarf members of the 4 Gyr-old open cluster M67 as calibrators for gyrochronology and tests of stellar spin-down models. Using *Gaia* EDR3 astrometry for cluster membership, and Pan-STARRS (PS1) photometry for binary identification, we build this set of rotation periods from a campaign of monitoring M67 with the Canada France Hawaii Telescope's MegaPrime wide field imager. We identify 1807 members of M67, of which 294 are candidate single members with significant rotation period detections. Moreover, we fit a polynomial to the period versus color-derived effective temperature sequence observed in our data. We find that the rotation of very cool dwarfs can be explained by simple solid body spin down between 2.7 and 4 Gyr. We compare this rotational sequence to the predictions of gyrochronological models and find that the best match is Skumanich-like spin-down, $P_{\rm rot} \propto t^{0.62}$, applied to the sequence of Ruprecht

147. This suggests that, for spectral types K7 to M0 with near-solar metallicity, once a star resumes spinning down, a simple Skumanich-like relation is sufficient to describe their rotation evolution, at least through the age of M67. Additionally, for stars in the range M1–M3, our data show that spin-down must have resumed prior to the age of M67, in conflict with the predictions of the latest spin-down models.

## 2.1 Introduction

A critical piece of understanding the evolution of any system—be it stars, planets, or the Milky Way galaxy itself, is understanding both the order in which events occur as well as their timescales. To do this properly one requires precise, reliable ages for the stars involved. M dwarfs are the most numerous stars in the galaxy (Gould et al. 1996; Bochanski et al. 2010), and have higher occurrence rates of small planets compared to higher mass stars (Dressing & Charbonneau 2015; Hardegree-Ullman et al. 2019). They also do not fuse heavy elements, and many tens of Gyr must pass before they show perceptible signs of evolution on a Hertzsprung-Russell diagram (Laughlin et al. 1997). As a result, M dwarfs can serve as particularly excellent tracers of galactic chemical evolution.

However, M dwarfs are also resistant to most methods commonly used for measuring a star's age. Their evolution on the main sequence is undetectable (Laughlin et al. 1997), there are no observable asteroseismic oscillations (Chaplin et al. 2011; Berdinas et al. 2017; Mathur et al. 2019), and their deep convective envelopes burn Li within the first $\sim$ 50 Myrs (Bildsten et al. 1997). The age-peculiar velocity relation is only statistical, making it unreliable for individual stars, and it breaks down for stars that are too young or too old (Aumer & Binney 2009; Lu et al. 2021). The age-metallicity relationship for the Milky way has flattened out over the past few Gyrs (Holmberg et al. 2007).

Fortunately, rotation period-age relations, or *gyrochronology*, show promise for M dwarf age-dating (Barnes 2003). Gyrochronology relies on the fact that a star spins down over time due to the interaction of its magnetic field with stellar winds, causing a loss of angular

momentum (Weber & Davis 1967; Skumanich 1972; Barnes 2007). Observations of Sun-like stars have shown that this angular momentum loss rate, $\frac{dJ}{dt}$, scales strongly with the angular rotation velocity ($\omega$) of the star, $\frac{dJ}{dt} \propto \omega^3$ (Skumanich 1972; Kawaler 1988; Mamajek & Hillenbrand 2008; Meibom et al. 2009; Angus et al. 2015; Gallet & Bouvier 2015), and as a result a star's initial rotation period ($P_{\rm rot}$) becomes less important with age (Epstein & Pinsonneault 2014; Gallet & Bouvier 2015). The availability of independent age-dating techniques for Sun-like stars such as asteroseismology and isochrone analysis has facilitated the calibration of this age-rotation relationship. This can be extended to M dwarfs but requires coeval populations of stars (i.e. clusters) of established ages in which the rotation periods of M dwarfs can be obtained.

The rotation period of a star as it hits the main sequence largely depends on two factors: the rotation period the star was born with ($P_{\rm init}$) and the protostellar disk lifetime. Using observations of the youngest pre-main-sequence clusters to fix the values of $P_{\rm init}$ indicates that slower rotators are likely to originate from longer disk lifetimes (Somers et al. 2017; Roquette et al. 2021). The diversity of $P_{\rm init}$ values and disk lifetimes leads to a spread of rotation periods ($\sim 0.2 - 8$ days) at the zero age main sequence. Regardless of the rotation period a star has once it reaches the main sequence, the evolution is dominated by spin down. As these stars forget their initial conditions they converge onto the slow rotator sequence, a well-defined sequence in temperature-period space. Prior to this the presence of any stars on a fast rotator sequence or those still heavily-influenced by their $P_{\rm init}$ value will make any rotation-age relation ambiguous. Since accurate gyrochronology relies on a star's initial rotation period becoming less important over time, it relies on convergence onto the slow rotator sequence.

One of the mechanisms by which these fast rotators delay their convergence is saturated spin down. Saturated spin-down occurs for stars with rotation rates greater than a critical value ($\omega_{\rm crit}$, a function of mass; Epstein & Pinsonneault 2014), where spin down scales as $\frac{dJ}{dt} \propto \omega \cdot \omega_{\rm crit}^2$ (Krishnamurthi et al. 1997). This is driven by a saturation of magnetic activity, which can be quantified using the Rossby number (Ro) defined as $(\omega\tau_{\rm cz})^{-1}$, where

$\tau_{\rm cz}$ is the convective overturn timescale. Generally, smaller Rossby numbers indicate that a star is more magnetically active. However, below a certain value (Ro $\lesssim 0.1$) stars appear to reach a maximal amount of activity, where decreasing values of Ro no longer correspond to increases in magnetic activity indicators (Wright et al. 2011; Matt et al. 2015, and references therein). This indicates that particularly fast rotators undergo a decoupling of their rotation rate and their magnetic field strength, resulting in a weaker scaling of torque with rotation rate. Because $\tau_{\rm cz}$ increases with mass, M dwarfs can remain in the saturated regime longer than their higher mass counterparts, which can be seen in the high number of M dwarf fast rotators in clusters such as Praesepe ($670 \pm 67$ Myr Douglas et al. 2017; Rebull et al. 2017) and the Hyades ($728 \pm 71$ Myr Douglas et al. 2019). Knowing when these fast rotators finally converge is critical for M dwarf gyrochronology.

Observations of solar-mass stars younger than the Hyades ($\lesssim$ 600 Myr) have shown that models which assume the entire star rotates with a uniform angular velocity (i.e., solid body rotation) fail to match the observed convergence onto a slow rotator sequence and subsequent evolution (Keppens et al. 1995; Krishnamurthi et al. 1997; Allain 1998). Models which incorporate the internal transport of angular momentum (i.e., differential rotation) relax the assumption of solid body rotation. In particular, core-envelope decoupling models take a simplified approach of treating the core and envelope as two separate, rotationally solid bodies with a mechanism that transports angular momentum between the two (MacGregor & Brenner 1991; Denissenkov et al. 2010; Lanzafame & Spada 2015). The critical parameter, then, is the timescale over which torques act to equilibriate the rotation rates ($\tau_{\rm c-e}$). Fits to cluster data have shown $\tau_{\rm c-e}$ is $\sim 20$ Myr for solar-mass stars and a strong function of mass ($\tau_{\rm c-e} \propto M^{-7.28}$ or $M^{-9.1 \pm 1.8}$ by Lanzafame & Spada 2015; Somers & Pinsonneault 2016, respectively).

Recent observations of a collection of open clusters, namely Praesepe (Douglas et al. 2017; Rebull et al. 2017), the Hyades (Douglas et al. 2019), NGC 6811 (Curtis et al. 2019), and NGC 752 (Agüeros et al. 2018), have shown that K and early M dwarfs appear to halt their spin down for a period of time—a striking departure from a standard spin-down

model with solid body rotation, but a phenomenon that can be explained by core-envelope decoupling models (Spada & Lanzafame 2020). In Spada & Lanzafame (2020) the apparent stalling is caused by the angular momentum loss of the envelope being balanced by transport from the core. The result is a net loss of angular momentum from the star, while the envelope continues to rotate at a roughly constant rate. However, their model does not predict the same degree of stalling as observed in open clusters, as it predicts that stars later than K5 should be rotating $\sim 5$ days slower than they are in Ruprecht 147 (Curtis et al. 2020). We know that K and M dwarfs must resume spinning down, as field samples show K and M dwarfs with rotation periods that are many tens of days (McQuillan et al. 2013; Newton et al. 2016, 2017; Santos et al. 2019). Such rotation periods are roughly consistent with a Skumanich-type spin-down over the age of the galactic disk (van Saders et al. 2019). Knowing when these stars resume spinning down and the timescales over which internal angular momentum exchange occur both directly affect the mapping of a rotation period to an age.

Calibrating gyrochronology and testing spin-down models for M dwarfs requires a larger sample of older, well-dated M dwarfs. Only a handful of such stars are currently available, the majority of which are in young clusters (700 Myr at the oldest; Douglas et al. 2017; Rebull et al. 2017) or are limited by the use of kinematic ages (Newton et al. 2016; Popinchalk et al. 2021). Previously, Barnes et al. (2016) used *K2* to obtain calibrators for gyrochronology of solar-type stars in M67, but observing faint M dwarfs in crowded fields has proved impossible for missions such as *K2* or *TESS*. The Canada France Hawaii Telescope's MegaPrime (Boulade et al. 2003) instrument allows us to overcome the limitations of *K2* and *TESS* in sensitivity, without significant loss in field-of-view. In this paper we present the rotation periods of late K and early M dwarf members of the 4 Gyr-old cluster M67 (3.5-5.0 Gyr; Nissen et al. 1987; Demarque et al. 1992; Montgomery et al. 1993; Carraro & Chiosi 1994; Fan et al. 1996; VandenBerg & Stetson 2004; Balaguer-Núñez et al. 2007; Stello et al. 2016). We present the oldest K and M dwarf gyrochrone to date and compare it to literature gyrochronology relations.

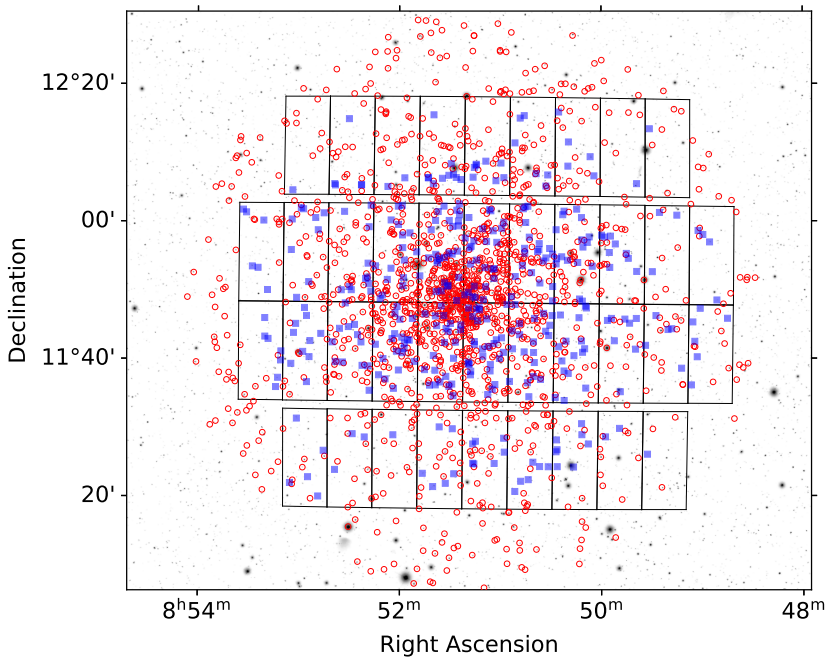


Figure 2.1: A Sloan Digital Sky Survey DR9 $i$-band image of the M67 field, with all of our candidate M67 cluster members identified by circles. Blue circles identify the the stars with reported rotation periods in Table 2.2. The black boxes are the MegaPrime footprint for one of the pointings in our dither pattern.

## 2.2 Observations and Data Reduction

Our campaign used Canada France Hawaii Telescope's (CFHT) MegaPrime to monitor M67 (center coordinates: $\alpha = 8^{\rm h}51^{\rm m}18^{\rm s}$, $\delta = +11°48'00''$) from 2018 October 15 to 2021 March 5 (UT). MegaPrime is the MegaCam imager placed at the prime focus of CFHT; it has a 1 square degree field-of-view sampled by 40 CCDs arranged in 4 rows of 9, 11, 11, and 9 detectors each (Fig. 2.1). In total we obtained 694 exposures of the cluster in discrete 1-2 week runs, producing 131 epochs of data for our light curves. All data were collected with 121 second integration times using the Sloan $i$ filter, red enough that M dwarfs are not too faint but blue enough to observe spot variability. Observations were taken five at a time in a cross-like dither pattern with 10.4 arcsec offsets. Bias subtracting, flat-fielding, fringe correction, and bad-pixel masking were all performed by version 3.0 of the CFHT `Elixir` pipeline (Magnier & Cuillandre 2004). For our data reduction we treated the five

exposures in a dither pattern independently, only combining them when we averaged the five photometric measurements together in the later steps of the pipeline. An image of the field taken from $i$-band images of the Sloan Digital Sky Survey DR9 is shown in Fig. 2.1. Included are the candidate cluster members of M67 (see Sec. 2.3 for further details).

### 2.2.1 Sky Background

We started with determining and removing the sky background from each detector's image. For this we used `MMMBackground`, a `python` implementation of the DAOPHOT MMM algorithm contained in the `photutils` package (Stetson 1987; Bradley et al. 2020). We divided each image into a 8x10 grid of equally sized sub-regions and for each sub-region we estimated the background level through an estimation of the mode by the equation $Mode \approx 3 \times Median - 2 \times Mean$. This 8x10 grid was then interpolated to the size of the original image using a bi-cubic spline and the resulting sky background was subtracted from the image. To estimate the uncertainty on this sky background we also computed the sigma-clipped standard deviation of each sub-region in the grid which was similarly interpolated to produce an estimated uncertainty for each pixel in the sky background.

### 2.2.2 Source Finding

With the sky background subtracted, we then used `DAOStarFinder`, a `python` implementation of the DAOFIND algorithm in the package `photutils`, to find the location of every source in the field for each individual image (Stetson 1987; Bradley et al. 2020). The threshold was set relatively low, at three times the sigma-clipped standard deviation of all pixel values in the image, and the full width at half maximum (FWHM) was set at the seeing value reported in the image header. Using the World Coordinate System values in the image headers, we converted the pixel coordinates reported by `DAOStarFinder` to RA and Dec (J2000.0). This enabled us to cross-match our detected sources with external catalogs.

We downloaded a catalog of every *Gaia* EDR3 (Gaia Collaboration et al. 2021) source in the field of view and converted the RA and Dec coordinates to the epoch J2000.0. For each *Gaia* source we then found the nearest neighbor match reported by `DAOStarFinder`. A handful of *Gaia* sources did not have a detection within the cut-off of 0.75 arcsec and were considered non-detections. Any remaining sources found by `DAOStarFinder` that were not paired up with a *Gaia* source were considered false positives and discarded from our catalog. A nearest neighbor search, with the same distance cut-off, was also used to match every *Gaia* source to a Pan-STARRS1 (PS1) DR2 source. After this cross-matching our catalog contained 8287 sources, all of which were matched to a source in both *Gaia* EDR3 and PS1 DR2. The limiting magnitudes of our observations ($i \sim 21$) compared to that of *Gaia* EDR3 ($G \sim 21$) and PS1 DR2 ($i \sim 22$) limit the number of real sources that were discarded by this method.

### 2.2.3 Photometry

Next we performed aperture photometry on the background-subtracted images for every source in our catalog. The aperture diameter was set at four times the seeing value for the image, a value computed from the average empirical full width at half maximum of bright sources scattered throughout the field. This diameter was chosen after analyzing the effect of aperture size on the noise properties of the light curves (see related discussion in Sec. 2.2.4). Any sources with overlapping apertures were flagged and excluded from the calculation of the zero-point corrections described in this section due to the source confusion introduced by their overlap. Instrumental magnitudes were computed by a sum over the aperture divided by exposure time, and an uncertainty was estimated from the quadrature sum of: the photon noise on the flux in the aperture, the read noise of the MegaPrime detectors, and the previously estimated sky uncertainty for each pixel in the aperture. With this process repeated for each of our observations, we then began constructing the light curves for each target.

In order to construct the light curves we first averaged together the measurements within an epoch (i.e., the set of five exposures that make up one dither pattern). To do this we corrected for small changes in the photometric zero-point that may have occurred between exposures. The correction, which we call $\Delta_i$, was taken to be the median difference between the stars with low scatter in their instrumental magnitudes. In equation form, the correction applied to the $i$th observation relative to the first ($i = 0$) is given by:

$$\Delta_i = \text{Median}\,(M_{ls,0} - M_{ls,i}) \tag{2.1}$$

Where $M_{ls,i}$ represents the set of stars with less than median scatter in their $n$ measurements. Since any measurement where the aperture included bad pixels is discarded, $n \leq 5$. The epoch magnitude was then computed from the average of the zero point-corrected measurements. If $m_i$ is the instrumental magnitude from the $i$th observation within the $j$th epoch then $\bar{m}_j$, which will become a point in a light curve, is given by:

$$\bar{m}_j = \frac{1}{n}\sum_{i=0}^{n-1}(m_i + \Delta_i) \tag{2.2}$$

We repeated this calculation for every star and every epoch.

Finally, we corrected for the changes in the photometric zero-point between epochs. We took the same approach as before, computing this correction from the low scatter stars. The zero-point correction, $\text{zp}_j$, of the $j$th epoch relative to the first ($j = 0$) is given by:

$$\text{zp}_j = \text{Median}(\bar{M}_{ls,0} - \bar{M}_{ls,j}) \tag{2.3}$$

Where $\bar{M}_{ls,j}$ represents the set of stars with less than median scatter in their computed $\bar{m}$ values. Each $\bar{m}$ was then corrected by this zero-point correction:

$$m_{\text{epoch},j} = \bar{m}_j - \text{zp}_j \tag{2.4}$$

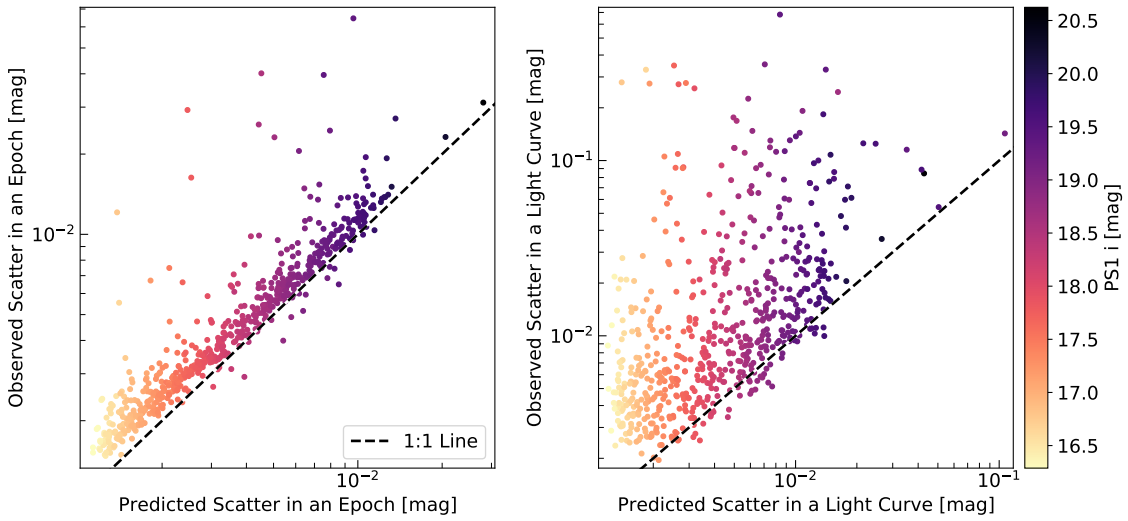


Figure 2.2: **Left Panel**: A scatter plot of the predicted versus observed scatter of the zero-point corrected magnitudes that are averaged together to form one epoch in our light curves. The expectation is that these points lie on the one-to-one line. **Right Panel**: A scatter plot of the predicted versus observed scatter of the zero-point corrected magnitudes in our light curves, the one-to-one line is the expected lower-limit. In both panels the predicted values are derived from our estimated uncertainties.

In total, we obtained 4396 light curves that met our completeness criterion of at least 99 epochs of available data (see Sec. 2.4 for further details).

### 2.2.4 Validation

In order to validate our model of the photometric noise we performed a comparison of the observed scatter in the zero-point corrected magnitudes to the scatter expected from the estimated uncertainties alone. We made two important assumptions for these tests: 1) the uncertainties were the standard deviation of independent Gaussian distributions, and 2) all of these distributions had the same mean (i.e., the uncertain measurement was the only source of variability). Thus, any sources with additional variability in their magnitudes would fall above the one-to-one line on a plot of the theoretical scatter versus the observed scatter.

First, we performed this test on the $n \leq 5$ measurements that form an epoch, comparing the standard deviation of these points to the scatter expected from the uncertainty on their average. Exposures in an epoch were collected over a period of roughly 20 minutes, short enough that we expected each star not to vary. As a result, a scatter plot of how the noise was modeled versus the observed scatter should follow a one-to-one line, as we see in our data (left panel of Fig. 2.2). For sources with magnitudes of $i \lesssim 18$, the data show a departure from the one-to-one line which we attribute to either non-linearity in the detector as it approaches saturation or a fractional measurement error, such as flat fielding errors.

Second, we performed this test on full light curves, comparing the standard deviation of the epoch magnitudes to the scatter expected from their uncertainties. The one-to-one line is expected to be the lower limit of photometric scatter, therefore many sources will show variability beyond the case of random variations due to uncertain measurements of the magnitude. We stress that a source falling above the one-to-one line in the right panel of Fig. 2.2, meaning it has more variability than expected from uncertainty in the photometry alone, is not proof of the source having an astrophysical process driving that variability. That the one-to-one line is indeed the lower limit in the right panel of Fig. 2.2 demonstrates that our model of the noise is correct.

## 2.3 Cluster Membership and Stellar Properties

An important aspect of the results presented in this paper is that the rotation periods reported can be used as benchmarks for stellar spin down models. Critical to this is knowing the age and $T_{\rm eff}$. The age determination comes from their membership in the open cluster M67, whose age has been previously determined to be 4 Gyr (3.5–5 Gyr; Nissen et al. 1987; Demarque et al. 1992; Montgomery et al. 1993; Carraro & Chiosi 1994; Fan et al. 1996; VandenBerg & Stetson 2004; Balaguer-Núñez et al. 2007; Stello et al. 2016). The effective temperatures are derived using a color-$T_{\rm eff}$ relation. In this section, we provide the details on both of these critical aspects.

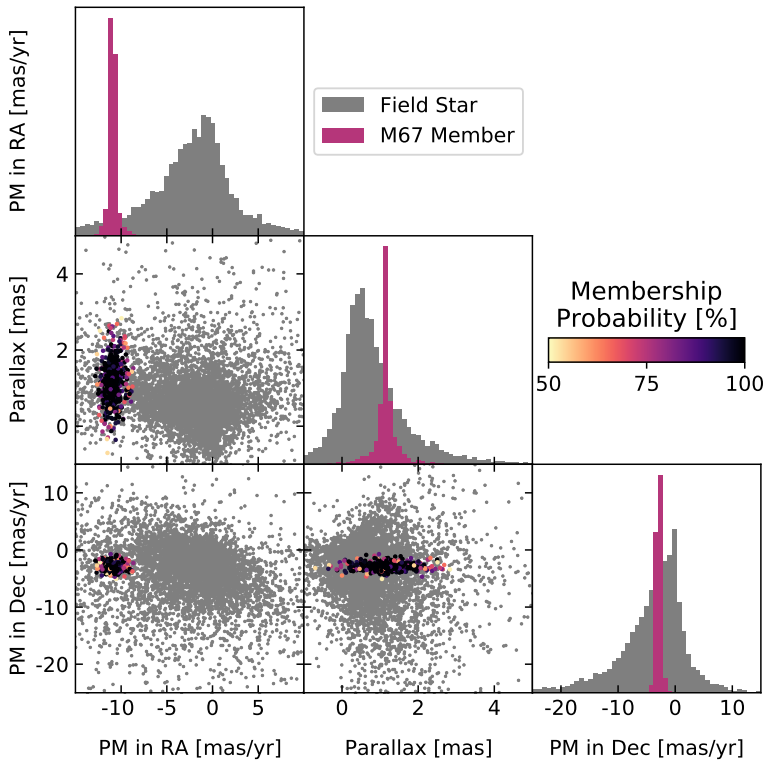


Figure 2.3: Scatter plots and histograms of the three parameters used for cluster membership determination (proper motions, or PM, in RA and Dec, and parallaxes). In gray, the distribution of these parameters for the non-cluster stars as a point of comparison. For cluster members color indicates the probability of membership, showing that the members on the "outskirts" of the distribution are less likely to be considered members of M67 (see Sec. 2.3.1 for further details).

### 2.3.1 Cluster Membership

Cluster membership was determined by using a clustering algorithm, `HDBSCAN` (McInnes et al. 2017), on *Gaia* EDR3 proper motions and parallaxes for every star in the MegaPrime field of view, regardless of whether or not it appeared in our catalog of light curves. `HDBSCAN` works by using the density of points to estimate a probability distribution function (PDF) that describes the full distribution of values in the data. Clusters are then defined by the peaks in this PDF. The primary advantage of `HDBSCAN` is that it relies on fewer assumptions about the data than more traditional clustering algorithms such as K-means, which assumes Gaussian distributions. It also does not require that every point in the data set be assigned

to a cluster, reducing the risk that outlier field stars might incorrectly be assigned M67 membership. The `python` package of the same name provides many different parameters to tune the performance of the clustering[1]. We found that the defaults for the version we used, v0.8.18, were acceptable with one exception: `min_samples`. This parameter can be thought of as determining the level of detail in `HDBSCAN`'s estimation of the underlying PDF. Too small a value and each data point produces its own peak in the estimated PDF, too large and the finer details of the estimated PDF are washed out. Given that the distribution of parallaxes and proper motions is effectively a two-peaked distribution (Fig. 2.3) we found that a value of 200 gave suitable clustering results compared to the default of 5.

A disadvantage of the `HDBSCAN` algorithm is that it does not make use of the uncertainties on any input data. To incorporate these into our cluster membership determination we performed Monte Carlo sampling. We ran the clustering algorithm on our list of *Gaia* sources, recorded the results, and resampled every star assuming Gaussian uncertainties, repeating this process 1000 times. `HDBSCAN` cannot be instructed to find a cluster with specific properties, so with each realization we computed the median parallax and proper motions for each grouping it found in the data and used the one with the closest match to literature values for M67 ($\pi = 1.1327 \pm 0.0018$ mas, $\mu_\alpha \cos\delta = -10.9738 \pm 0.0078$, $\mu_\delta = -2.9465 \pm 0.0074$ mas yr$^{-1}$; Gao 2018). The difference was never more than a few percent. We then calculated a "kinematic membership probability" from the fraction of realizations in which a star was assigned membership to M67. A final membership criterion of $> 50\%$ was selected based on an inspection of the *Gaia* color-magnitude diagrams (CMDs, Fig. 2.4) that were produced for various thresholds.

Another aspect we considered in our use of `HDBSCAN` was the Bayseian nature of this approach. Too small a field of view and the algorithm may not have had the leverage needed to separate M67 members from the field, too large and the diversity of field stars may have encouraged labelling true members as field stars. To address this we repeated our membership determination on a *Gaia* EDR3 catalog including stars out to twice the

[1]Details on the parameters can be found under Parameter Selection for HDBSCAN* (`https://hdbscan.readthedocs.io/en/0.8.18/`) in the docs

radius of the MegaPrime field of view and compared the two membership lists. Of the 1807 members within the MegaPrime field of view 76 were considered field stars when using the larger catalog, and none of the field stars gained membership in M67. None of these 76 stars are outliers on our CMDs (Fig. 2.4), so we have kept them in our final list of members. However, we flagged them as potentially suspect, so that the interested reader may remove them from the sample if they wish.

We compared our list of M67 members to that of Gao (2018), who applied a Gaussian mixture model based approach to *Gaia* DR2 astrometry. They found a list of 1502 likely members, whereas we have found 1807. In common between the two catalogs are 1241 members, leaving 261 stars that are unique to the Gao (2018) catalog, and 566 that are unique to our catalog. There are several factors that contributed to these differences. First, our search for members was limited to the field of view of CFHT MegaPrime, and this truncated our search at a radius of $\sim$30 arcminutes; all 261 stars that are only in the Gao (2018) catalog were outside our field of view and thus were not included in our clustering. Second, 431 of the 566 stars that appear only in our catalog have parallaxes and/or proper motions that are closer to the literature values for M67 in EDR3 than in DR2. Third, 99 of the 566 stars that appear in our catalog are new in EDR3 and thus could not have been included in the Gao (2018) catalog. Finally, there are 36 stars which are unique to our catalog for otherwise unknown reasons, we attribute these to the differences between the two methods used. The members that our two catalogs have in common are denoted by the "Gao member" column in Table 2.2.

### Single vs Binary Members

Unresolved binaries bias our inferred stellar parameters and close binaries have spin-down influenced by tidal forces (Simonian et al. 2020); as a result we also need to identify whether or not the M67 members have a companion. With a parallax of $\pi = 1.1327 \pm 0.0018$ mas, *Gaia* is able to resolve binaries that are separated by $\gtrsim 600$ AU. However, due to the size of our apertures stars with physical separations $\lesssim 7000$ AU have overlapping apertures. As

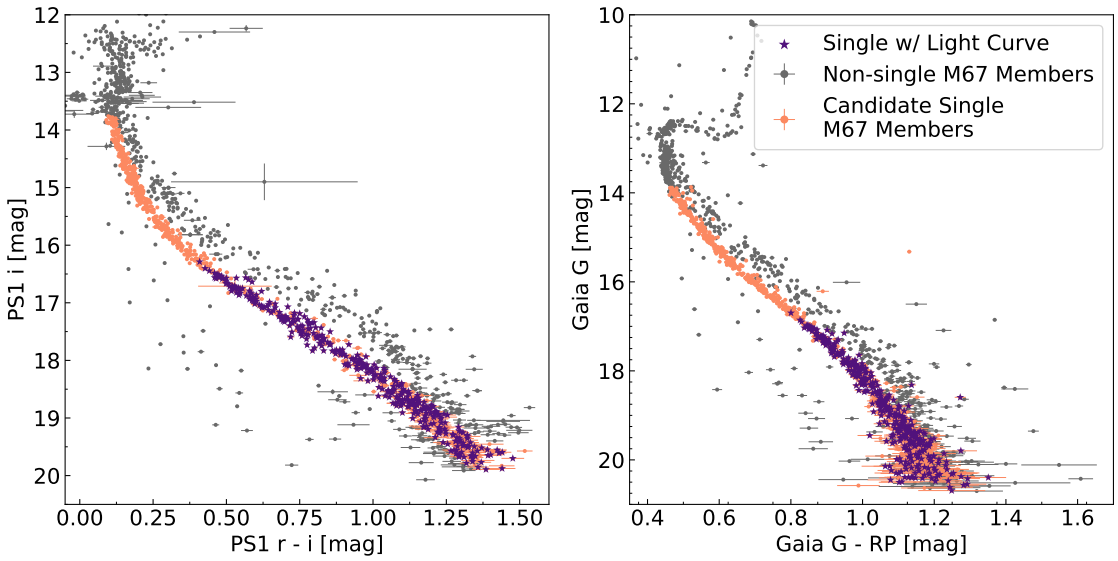


Figure 2.4: The color magnitude-diagram of kinematically selected M67 members. Left panel is using the Pan-STARRS DR2 photometry and right panel is using *Gaia* EDR3 photometry. In both panels orange points represent main sequence single members (subject to a brightness cutoff at lower magnitudes), grey points represent photometric binaries, and purple points indicate stars with rotation periods reported in our results.

such, their photometry was potentially limited by confusion with their nearest neighbor. For completeness, we included these stars in our catalog of reported rotation periods (Sec. 2.5), but we excluded them from our subsequent analysis. Work done by Deacon & Kraus (2020) indicates there are no wide binaries separated by $\gtrsim$ 3000 AU in clusters, thus our analysis was focused only on single members of M67. Binary systems which are not resolved require a different method of detection. Common approaches include: 1) spectroscopy that resolves double-lined absorption features, 2) excess astrometric noise (quantified by the renormalized unit weight error, or RUWE, for *Gaia* astrometric solutions; Belokurov et al. 2020), and 3) photometric excess, stars that appear brighter than the main sequence on a CMD. For our data we used the photometric excess approach, calculated from PS1 photometry (Magnier et al. 2020; Flewelling et al. 2020). The effectiveness of this approach was confirmed by the finding that all the sources which exhibited excess astrometric noise (i.e., RUWE $\gtrsim$ 1.4) were also found to show photometric excess.

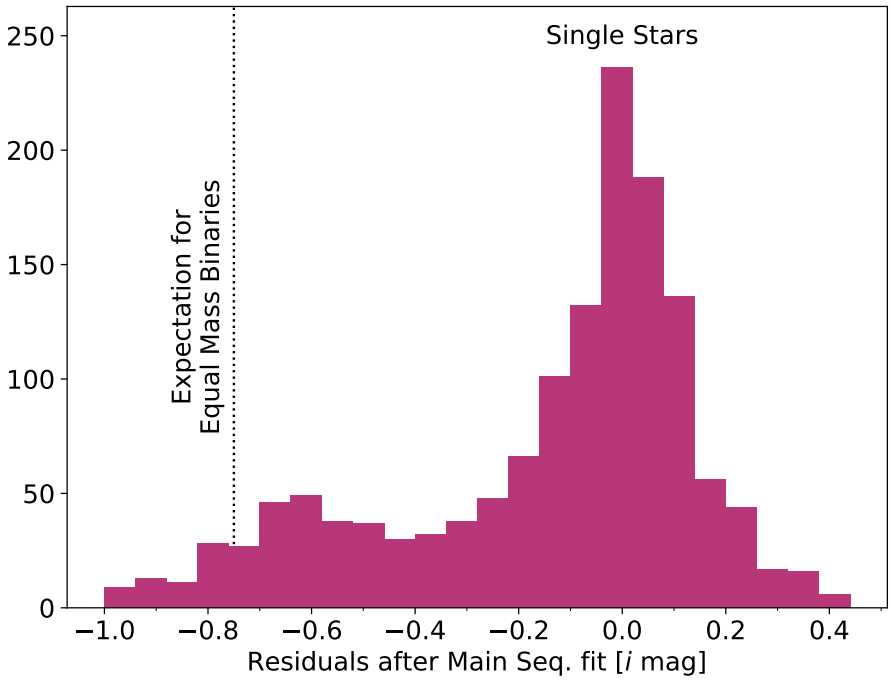


Figure 2.5: The distribution of residuals after subtracting out a polynomial fit to the main sequence from each star in the catalog. The shaded region denotes the stars chosen as single stars on the main sequence. The -0.3 offset represents the approximate location of the valley between the two peaks in this distribution, while accounting for the wide spread about the binary peak centered at $\sim -0.6$. The vertical dotted line denotes the expected excess brightness for equal mass binaries.

In PS1 DR2 the saturation limit is 12-14 magnitudes, depending on seeing and filter; for M67 we found that a cut at $i = 13.75$ removed these problematic sources. From the photometry in *Gaia* EDR3 and PS1 DR2 we found that PS1 $r$ and $i$ were the two filters with the highest signal-to-noise ratios for the faintest members in our catalog. Therefore, we used $3\sigma$ iterative outlier rejection to fit an eighth order polynomial to the main sequence of the cluster on a PS1 $r - i$ vs $i$ CMD. We then categorized each source by its vertical distance from the main sequence on the CMD based on the distribution of residuals after subtracting out our fit to the main sequence (Fig. 2.5). Stars within $\pm 0.3$ magnitudes of the main sequence fit were classified as single members, whereas sources outside these bounds were categorized as photometric binaries. The small secondary peak of binary members is broad, which suggests there may be a small number of high-contrast binaries contaminating our sample of candidate single M67 members. Sources fainter than the main sequence are thought to be binaries with a white dwarf component. Further observations are required to confirm this, which will be included in future work. The fraction of sources labeled as binaries by this method is 26%, in line with the expectation for M dwarf multiplicity rates (Duchêne & Kraus 2013; Winters et al. 2019). Both the PS1 $r - i$ vs $i$ CMD that was used for this binary classification and an additional *Gaia* $G - RP$ vs $G$ CMD can be seen in Fig. 2.4. The stars identified as binaries by this method were set aside for future analysis. They do not have rotation periods reported in this paper.

### 2.3.2 Effective Temperatures

In order to calculate the effective temperature ($T_{\rm eff}$) for the stars in our catalog we used a $(r - i)$ vs $T_{\rm eff}$ relation derived from the sample of late K and M dwarfs analyzed by Mann et al. (2015). We converted the synthetic Sloan $r$ and $i$ photometry provided into the PS1 $r$ and $i$ passbands using the Tonry et al. (2012) relations and applied corrections for reddening ($E(B-V) = 0.041 \pm 0.004$ mag; Taylor 2007) as well as a conversion to apparent magnitudes for the distance to M67 ($\pi = 1.1327 \pm 0.0018$ mas; Gao 2018). We trimmed the sample to stars with metallicities of $-0.07 \leq$ [Fe/H] $\leq 0.07$, a range chosen to cover various

Table 2.1: A description of the data for the M dwarfs used to derive $T_{\rm eff}(r-i)$ , available in a machine-readable format online.

| Name | Table Header | Units | Description |
|---|---|---|---|
| Object Name | `name` | – | Source name used in Mann et al. (2015) |
| Right Ascension | `raDeg` | ° | – |
| Declination | `deDeg` | ° | – |
| *Gaia* G magnitude | `gaiaGmag` | mag | The synthetic *Gaia* G magnitude |
| *Gaia* BP magnitude | `gaiaBPmag` | mag | The synthetic PS1 *Gaia* BP magnitude |
| *Gaia* RP magnitude | `gaiaRPmag` | mag | The synthetic PS1 *Gaia* RP magnitude |
| Mass | `solMass` | $M_\odot$ | Mass of the star |
| Error on the Mass | `e_solMass` | $M_\odot$ | – |
| Metallicity | `[Fe/H]` | – | Metallicity of the star |
| Error on the Metallicity | `e_[Fe/H]` | – | – |
| $T_{\rm eff}$ | `teff` | K | Effective Temperature |
| PS1 g magnitude | `ps1gmag` | mag | The synthetic PS1 g magnitude |
| Error on PS1 g magnitude | `e_ps1gmag` | mag | – |
| PS1 r magnitude | `ps1rmag` | mag | The synthetic PS1 r magnitude |
| Error on PS1 r magnitude | `e_ps1rmag` | mag | – |
| PS1 i magnitude | `ps1imag` | mag | The synthetic PS1 i magnitude |
| Error on PS1 i magnitude | `e_ps1imag` | mag | – |
| PS1 z magnitude | `ps1zmag` | mag | The synthetic PS1 z magnitude |
| Error on PS1 z magnitude | `e_ps1zmag` | mag | – |
| Ks magnitude | `Ksmag` | mag | The synthetic Ks magnitude |
| Error on Ks magnitude | `e_Ksmag` | mag | – |

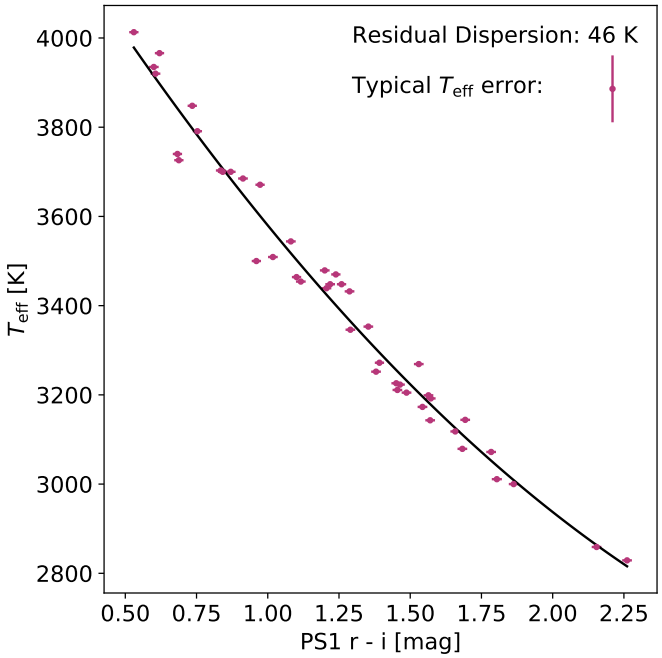


Figure 2.6: The sample of late K and M dwarfs of Mann et al. (2015) used to derive our color-$T_{\rm eff}$ relationship. We chose stars to have a metallicity within the range of literature values for M67. The $T_{\rm eff}$ errors are of order 75 K and do not affect the dispersion.

values reported for the metallicity of M67 in the literature (Pace et al. 2008; Santos et al. 2009; Önehag et al. 2011; Liu et al. 2016; Sandquist et al. 2018). The parameters of the trimmed sample are included in Table 2.1. Finally, we fit a second order polynomial to the $(r-i)$-$T_{\rm eff}$ pairs to obtain our relation:

$$T_{\rm eff} = 139.8(r-i)^2 - 1062.1(r-i) + 4502.1. \tag{2.5}$$

The residual dispersion of 46 K is small compared to the errors on the temperatures (Fig. 2.6). Adding this in quadrature with the spectroscopic errors provided by Mann et al. (2015) yields a $T_{\rm eff}$ uncertainty of $\sim 75$ K.

## 2.4 Measuring Rotation Periods

In our data set there are 7222 sources which contain at least one epoch of data. To reduce complications with recovering periodic signals we applied a conservative cut to our data, requiring that a light curve have a minimum completion of 99 out of the possible 131 epochs of data. After applying this cut we were left with a sample of 4674 stars, with a mean completeness of 129 epochs. Of these 4674 stars, 3607 have light curves with 131 epochs. For the 636 candidate cluster members that made these cuts the mean completeness is 128 epochs, with 444 having a light curve that has 131 epochs. Due to the irregular sampling of our light curves we used Lomb-Scargle (LS) periodograms (Lomb 1976; Scargle 1982; Press & Rybicki 1989; Zechmeister & Kürster 2009) for the detection of periodic signals in our light curves. In each case the rotation periods we report was the period of maximum power in the periodogram.

A common method for quantifying the uncertainty of LS periodograms is the false alarm probability (FAP). The FAP is a measure of probability that data with no signal would produce a peak in the periodogram of equivalent height (for further details see Sec. 7.4.2 of VanderPlas 2018). We required a FAP value of less than one percent for a periodic signal to be considered significant. To maintain the computational feasibility of our injection and

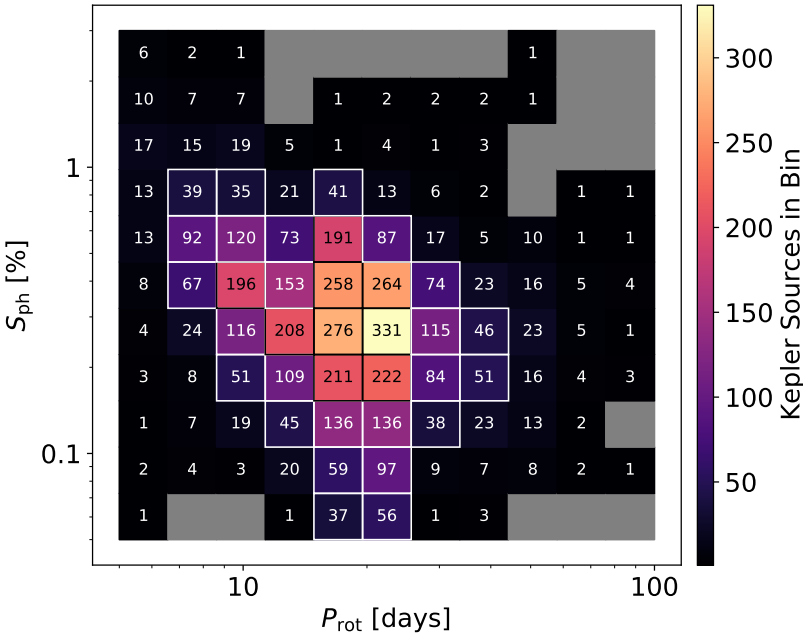


Figure 2.7: The number of *Kepler* light curves used in the injection and recovery tests to establish completeness as a function of rotation period ($P_{\rm rot}$) and photometric variability ($S_{\rm ph}$). Bins with a black or white (color chosen for optimal contrast) box drawn around them are the ones where over half (i.e. $\geq 25$) of the injected signals are *Kepler* light curves.

recovery tests (see Sec. 2.4.1) we report FAP values estimated using the Baluev (2008) method. As a test of the validity of using the Baluev estimates, we performed a comparison of the FAP values estimated by the Baluev method to those computed using a bootstrapping ($N = 10^4$) of all of our light curves. Using the bootstrapping method it is roughly expected to find FAP $\times$ $N$ $\pm$ $\sqrt{\text{FAP} \times N}$ false positives (VanderPlas 2018). Accounting for this uncertainty on the FAP value, every one of our Baluev estimated FAP values is consistent with its bootstrapped equivalent. We also required that a rotation period have at least five complete periods within the light curve duration in order to be considered a detection. This placed an upper limit of 175 days on any rotation periods used in our analysis.

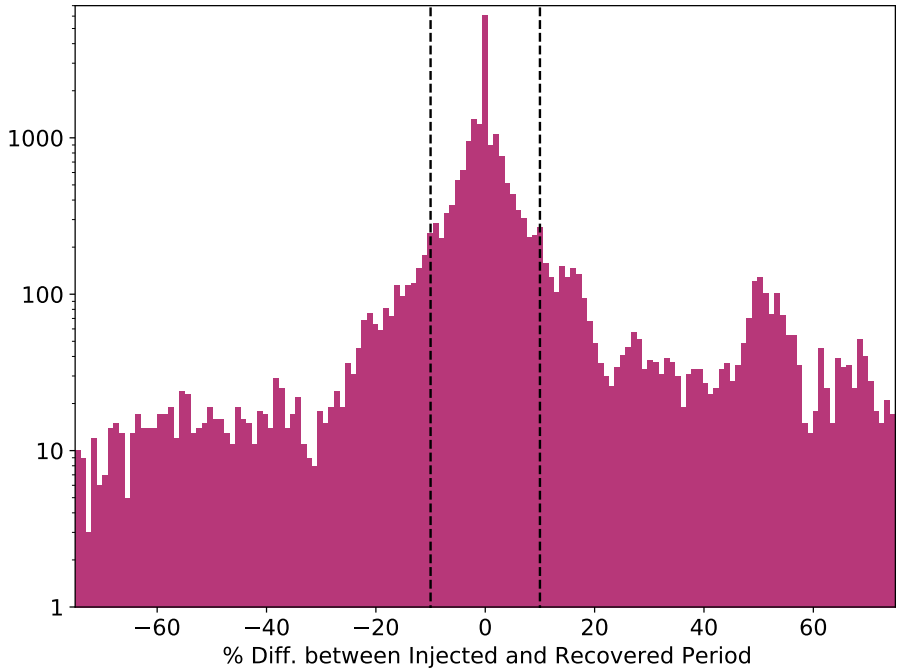


Figure 2.8: The distribution of the percent differences between the injected and recovered period (irrespective of the false alarm probability of the recovery). The precision on our rotation periods is set by the standard deviation of this distribution: 10%.

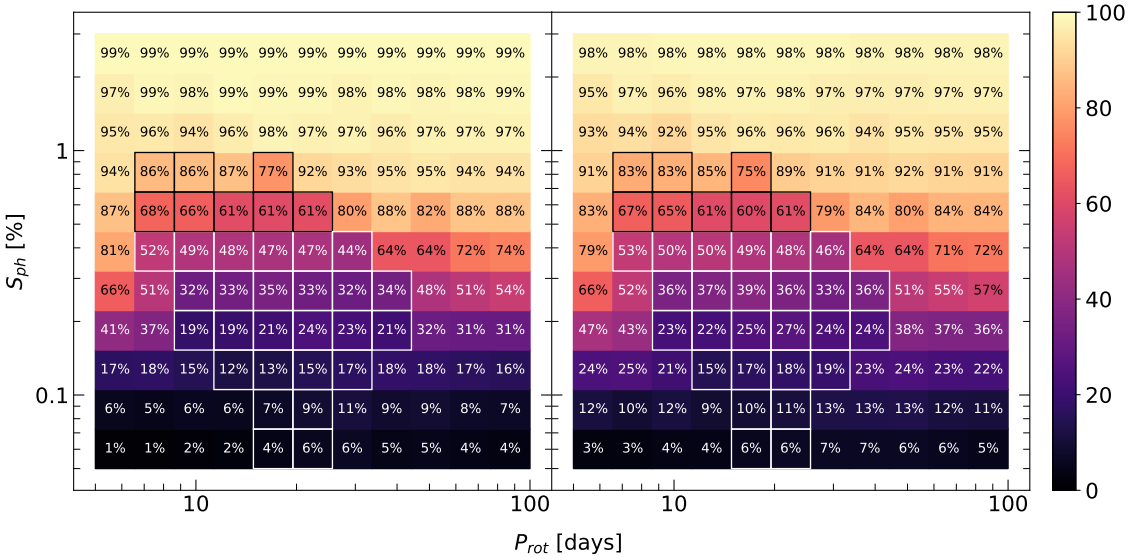


Figure 2.9: **Left Panel**: The recovery rate (%) of the period of the signal injected into a cluster member's light curve. **Right Panel**: Same as left panel, but for field stars rather than cluster members. The gradient from top to bottom demonstrates that the lower a signal's amplitude is, the harder it is to recover. In both panels bins with a black or white (color chosen for optimal contrast) box drawn around them are the ones where over half (i.e. $\geq 25$) of the injected signals are *Kepler* light curves.

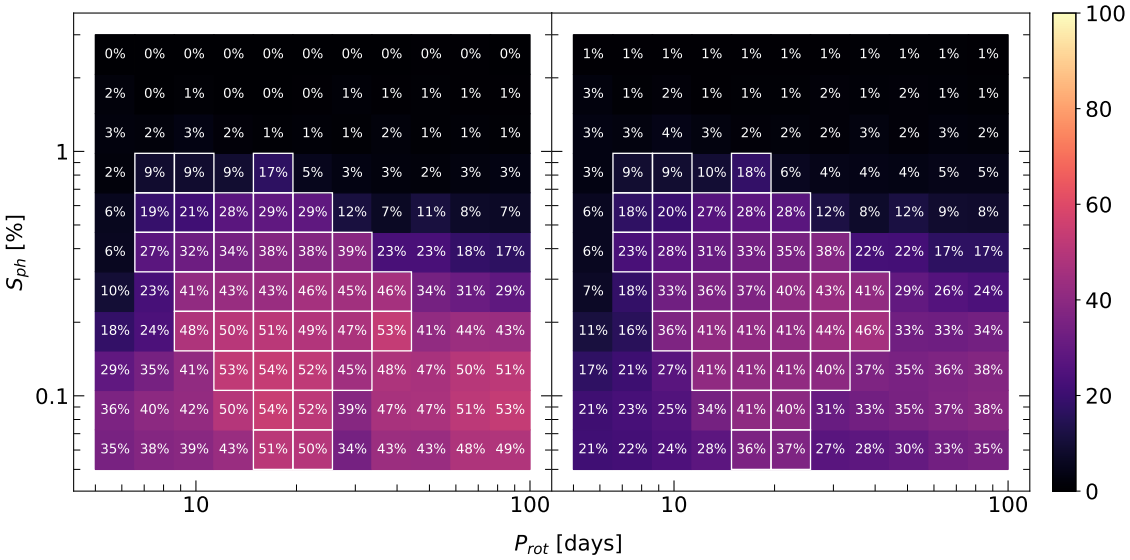


Figure 2.10: **Left Panel**: The percentage of the time we find a significant (FAP $< 0.01$) rotation signal but the period does not match what we injected into a cluster member's light curve (to within 10%). **Right Panel**: Same as the left panel, but for injections into a field star instead of a cluster member. Many of these light curves, especially those of the cluster members, already have periodic signals in them. Thus, in the case of a low amplitude injection we often recover what already existed in the data. Since this does not match what was injected, this is marked as a "false positive." In both panels bins with a white box drawn around them are the ones where over half (i.e. $\geq 25$) of the injected signals are *Kepler* light curves.

### 2.4.1 Injection and Recovery Tests

We performed injection and recovery tests to determine the detection efficiency and false positive rates for our recovered periods. The *Kepler* long-cadence data provided a database of real astrophysical signals of rotation for us to test our rotation recovery. For the injected signals, we used the KEPSEISMIC light curves of K and M dwarf main sequence stars obtained with the *Kepler* Asteroseismic Data Analysis and Calibration Software (KADACS; García et al. 2011, 2014; Pires et al. 2015). The rotation periods for these stars have been derived by Santos et al. (2019). We applied a few additional cuts of our own: first, we checked for the completeness of the *Kepler* light curve, rejecting any star with fewer than 11 continuous quarters of data. Second, we applied a cut on the height of the autocorrelation function peak ($H_{\rm ACF}$ in Santos et al. 2019, the average difference between the peak height and the two adjacent local minima) requiring that $H_{\rm ACF} \geq 1.0$, a value typical of stable signals. Finally, we applied a cut on the effective temperature of $T_{\rm eff} < 5270$ K, so that the observed spot pattern evolution in the *Kepler* sample would more closely match the expectation for our targets in M67. Given the precision of the *Kepler* photometry relative to our data, we made the assumption that these light curves contained noiseless rotation signals.

This gave us a sample of 4599 signals with known rotation periods for injection. Each signal was characterized by two values: the rotation period ($P_{\rm rot}$) and the photometric activity index ($S_{\rm ph}$), a measure of the amplitude of variability. The value of $S_{\rm ph}$ was calculated by dividing a light curve into sub-series, each five times the length of the star's rotation period, and then taking the mean of the standard deviations of each of the sub-series (Mathur et al. 2014). One the advantages of $S_{\rm ph}$ over other measures of photometric variability is its correlation with proxies of magnetic activity (Salabert et al. 2016, 2017). We created logarithmically spaced bins for the injections: $5 \leq P_{\rm rot} \leq 100$ [days] and $0.05 \leq S_{\rm ph} \leq 3$ [%Flux] using 11 bins along each axis. However, this left some of the outlier bins (see Fig. 2.7) with very few, if any, injections. To compensate for this deficiency we also generated a set of synthetic light curves. These synthetic light curves were simple

sinusoids:

$$\mathrm{Flux}(t) = \sqrt{2} S_{\mathrm{ph}} \sin\left(\frac{2\pi}{P_{\mathrm{rot}}} t + \phi\right). \tag{2.6}$$

Where $\phi$ is a uniformly distributed phase, and the factor of $\sqrt{2}$ comes from the fact that $S_{\mathrm{ph}}$ is calculated from a standard deviation. The synthetic light curves were sampled with the same cadence as the *Kepler* data. For every bin with less than 50 *Kepler* light curves we generated a sample of up to 50 synthetic ones with $P_{\mathrm{rot}}$ and $S_{\mathrm{ph}}$ values uniformly distributed (in linear space) within the bounds of that bin. In total we used 3934 synthetic light curves.

Each injection and recovery test involved taking a *Kepler* (or synthetic) light curve and sampling it to match the cadence and length of our CFHT observations. We then added the signal into one of our CFHT light curves and computed an LS periodogram for the combined data. If the period of maximum power in the resulting LS periodogram was within 10% of the injected period (see Fig. 2.8) and had an estimated FAP of less than 1%, then we considered this a successful recovery. If the period of maximum power was more than 10% different from the injected period and the estimated FAP was less than 1% we considered this a false positive. All other cases were considered non-detections. We did not want to assume that the period of maximum power in our periodograms was due to rotation, thus we did not remove any pre-existing signal from the light curves before injection. To prevent confusion with the signal already present in the CFHT lightcurves we removed any case where the injected period was within 10% of the signal already detected in the lightcurve. This filtered out no more than 11% of the tests in any given bin, with every bin having at least 45000 tests. This approach enabled us to incorporate the actual systematics present in our CFHT photometry that may have limited the recovery of periodic signals.

Since we are only interested in the rotation periods of the members of M67, we limited the sample of CFHT light curves to a subset of the candidate cluster members and a matching number of randomly selected field stars. We selected the light curves for the injection and recovery testing by applying three criteria. First, cluster members were required to have very high (i.e. = 1.0) membership probability, while field stars must have had very low (i.e.

= 0.0) membership probability. Second, they must have had at least 99 epochs of data available. Finally, they must not have had an overlapping aperture. We also required that the selected field stars have similar $r - i$ colors and apparent $i$ magnitudes to our selected cluster members, to mitigate the impact of any systematics that depended on color. This yielded 740 total light curves, 370 cluster members and 370 field stars, into which we injected each of our 4599 *Kepler* and 3934 synthetic light curves. Each injection and CFHT light curve pairing was repeated with three or four different phases, depending on how many CFHT light curves fit within the injection light curve. This was done to capture the shift in phase due to spot pattern evolution over the years of observations.

We compiled the results of these tests into our completeness diagram (Fig. 2.9) as well as our false positives diagram (Fig. 2.10). We have plotted the results from the cluster members and field stars separately. Injections into the light curves of cluster members served as a direct test of our ability to recover rotation signals in the cluster member data, while injections into the field stars served as a control sample. The underlying distribution of $P_{\rm rot}$ is different for each of these populations, and thus each is expected to impact the completeness diagram in different ways. Trends that are common to both figures are thus reflective of the pipeline's recovery capabilities in general. Any differences between the two panels that cannot be attributed to different $P_{\rm rot}$ distributions would reflect issues in the pipeline, but we do not see any such differences.

The completeness diagram (Fig. 2.9) shows the major trends we would expect: 1) as the amplitude of the rotation signal decreases our ability to recover the correct period also decreases, and 2) the evolving spot patterns in the *Kepler* light curves reduced our ability to recover the correct period. Our false positives diagram (Fig. 2.10) also shows the major trends that we expected. In particular we highlight the $10 - 20\%$ difference in false positive rates between cluster members and field stars for low amplitude injections ($S_{\rm ph} \lesssim 0.25\%$). Many of the light curves we injected signals into already had an existing periodic signal and, when injecting low amplitude signals we expected to instead recover the already present signal. This explains both the high percentage of false positives for low

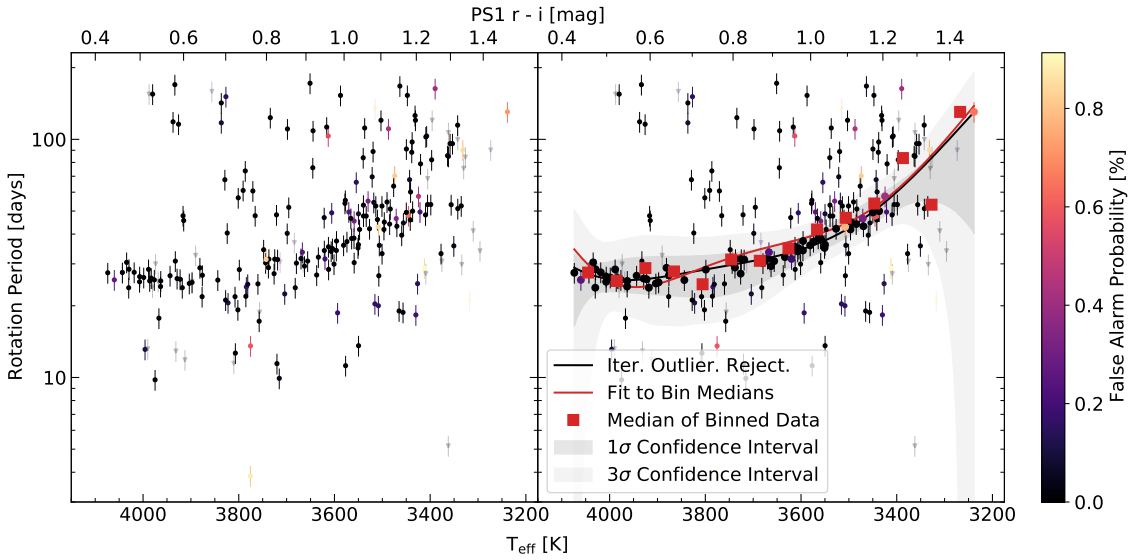


Figure 2.11: **Left Panel**: Recovered rotation periods for members of the open cluster M67 plotted versus their color-derived effective temperatures. All points have a low false alarm probability ($< 1\%$) for the detected rotation period. **Right Panel**: We fit a polynomial to the sequence by iterative outlier rejection. The larger points are used in the polynomial fit after outlier rejection. The shaded region is the confidence interval of this fit. Red squares are the median values of the data binned in $T_{\rm eff}$, and the red line is a polynomial fit to these values.

amplitude injections, as well as the difference in false positive rates. The cluster members were generally expected to show periodic variability due to their spot patterns. On the other hand, a smaller fraction of field stars were expected to show rotational variability and those that do span a much wider range of timescales (e.g., background evolved stars).

## 2.5 Results and Analysis

We present the full rotation catalog in Table 2.2. This information includes: *Gaia* EDR3 and PS1 DR2 source identifiers, the *Gaia* EDR3 astrometry and photometry, the PS1 DR2 *griz* photometry, the recovered rotation periods (if available), their estimated FAP values, the derived $T_{\rm eff}$ values, the percentage probability we calculated for M67 membership, and whether or not the star was flagged as a candidate binary. Appendix 2.8 contains plotted light curves and periodograms for each star in Table 2.2 with a reported rotation period.

Table 2.2: A description of the data for the Catalog of M67 Members , available in a machine-readable format online.

| Name | Table Header | Units | Description |
|---|---|---|---|
| *Gaia* Source ID | `gaiaid` | – | *Gaia* EDR3 `source_id` |
| Right Ascension (RA) | `RAdeg` | ° | – |
| Error on RA | `e_RAdeg` | mas | – |
| Declination (Dec) | `DEdeg` | ° | – |
| Error on Dec | `e_DEdeg` | mas | – |
| Parallax | `plx` | mas | – |
| Error on Parallax | `e_plx` | mas | – |
| Proper Motion in RA | `pmRA` | mas/yr | – |
| Error on Proper Motion in RA | `e_pmRA` | mas/yr | – |
| Proper Motion in Dec | `pmDE` | mas/yr | – |
| Proper Motion in Dec | `e_pmDE` | mas/yr | – |
| Renormalized Unit Weighted Error | `ruwe` | – | – |
| *Gaia* G Magnitude | `gaiaGmag` | mag | – |
| Error on *Gaia* G Magnitude | `e_gaiaGmag` | mag | – |
| *Gaia* BP Magnitude | `gaiaBPmag` | mag | – |
| Error on *Gaia* BP Magnitude | `e_gaiaBPmag` | mag | – |
| *Gaia* RP Magnitude | `gaiaRPmag` | mag | – |
| Error on *Gaia* RP Magnitude | `e_gaiaRPmag` | mag | – |

*continued on the next page*

Table 2.2, continued.

| Name | Table Header | Units | Description |
|---|---|---|---|
| PS1 Source ID | `ps1id` | – | Pan-STARRS1 DR2 `ObjID` |
| PS1 $g$ magnitude | `ps1gmag` | mag | – |
| Error on PS1 $g$ magnitude | `e_ps1gmag` | mag | – |
| PS1 $r$ magnitude | `ps1rmag` | mag | – |
| Error on PS1 $r$ magnitude | `e_ps1rmag` | mag | – |
| PS1 $i$ magnitude | `ps1imag` | mag | – |
| Error on PS1 $i$ magnitude | `e_ps1imag` | mag | – |
| PS1 $z$ magnitude | `ps1zmag` | mag | – |
| Error on PS1 $z$ magnitude | `e_ps1zmag` | mag | – |
| Probability of Membership | `memberprob` | – | Probability of Membership based on Kinematics (Sec. 2.3.1) |
| Photometric Single Star | `single` | – | Star was determined to be single (Sec. 2.3.1) |
| Photometric Binary | `binary` | – | Star was determined to be a multiple system (Sec. 2.3.1) |
| Member in Gao's M67 Catalog | `gaomember` | – | Star is also listed as a member by Gao (2018) |
| Potentially Suspect Member | `suspect` | – | Star's membership depended on catalog size (Sec. 2.3.1) |
| Used in Fit | `converged` | – | Is used in the polynomial fit after outlier rejection. |
| Effective Temperature | `teff` | K | Effective temperature derived from $(r-i)$ color (Sec. 2.3.2) |
| Rotation Period | `prot` | d | Rotation period derived from Lomb-Scargle Periodograms (Sec. 2.4) |
| False Alarm Probability | `fap` | – | The estimated false alarm probability of the rotation period |

We have plotted the measured rotation periods versus effective temperature for the 294 candidate single members of M67 with significant rotation detections in Fig. 2.11. For the analysis, we applied two extra cuts on the rotation periods, requiring that the stars have not been flagged as having an overlapping aperture (Sec. 2.2.3) or as a field-of-view dependent member (Sec. 2.3.1). Despite some scatter in the periods, they are concentrated about a locus in $T_{\rm eff}$-$P_{\rm rot}$ space. In an effort to describe this sequence, we performed a polynomial fit to the data using iterative outlier rejection, where at each step outliers were defined as the data greater than three median absolute deviations away from the median of the residuals. We did this for both $T_{\rm eff}$ vs $P_{\rm rot}$ and PS1 $(r-i)$ vs $P_{\rm rot}$, finding that both approaches converged to the same solution: a subset of 64 stars, for which the least-squares best fits are:

$$P_{\rm rot}(T_{\rm eff,4K}) = 9.66{\times}10^{-10}{\cdot}T^4_{\rm eff,4K}{+}8.25{\times}10^{-7}{\cdot}T^3_{\rm eff,4K}{+}2.69{\times}10^{-4}{\cdot}T^2_{\rm eff,4K}{+}0.016{\cdot}T_{\rm eff,4K}{+}25.9, \tag{2.7}$$

or

$$P_{\rm rot}(r-i) = 292\cdot(r-i)^4 - 895\cdot(r-i)^3 + 1054\cdot(r-i)^2 - 543\cdot(r-i) + 127.9, \tag{2.8}$$

where $T_{\rm eff,4K} = T_{\rm eff} - 4000$ K. We used bootstrapping (N=10000) to calculate confidence intervals about our fit, fitting a polynomial to 64 stars sampled with replacement from the 253 stars that passed all quality cuts. As a point of comparison, we have also taken the approach of binning the 253 stars in $T_{\rm eff}$, computing a median $P_{\rm rot}$ for each bin, and fitting a polynomial to these medians. The medians are plotted as red squares in Fig. 2.11, and their fit is plotted as a red line, which we have found is in agreement with the iterative outlier approach. We favor the results of the iterative outlier rejection due to its exclusion of points we believe are aliases from the fit to the $T_{\rm eff}$ vs $P_{\rm rot}$ sequence (see related discussion in Sec. 2.5.2).

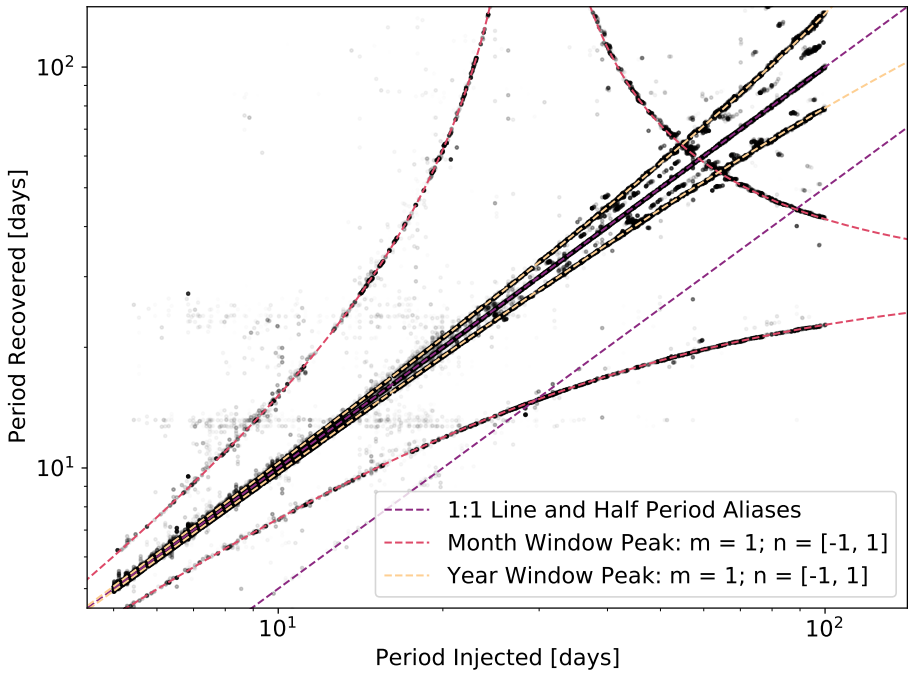


Figure 2.12: A scatter plot of the injected period vs the recovered period for one CFHT light curve. Each point represents the result of one *Kepler* (or synthetic) light curve being added to this cluster member's light curve. Low amplitude injections are dominated by the existing signal in the data, resulting in the horizontal features on this diagram. Dashed lines represent the 1-to-1 line for successful recoveries and the most prominent window function effects: half period aliasing and the Month and Year window peaks (see Sec. 2.5.1 for detailed discussion). Additional peaks in the window function align with other trends in this figure but are not plotted to reduce figure crowding (e.g., $m = 1$, $n = \pm 1$ and $\delta P \sim 180$ would fall between the plotted year-based effect and the 1:1 line).

### 2.5.1 Lomb-Scargle Failure Modes

In addition to the 10% uncertainties determined from our injection and recovery tests (Sec. 2.4.1) there are systematic uncertainties contributing to the scatter in our results (Fig. 2.11). These are the failure modes of the LS periodogram, originating from the irregular sampling in time. For the purposes of this discussion we will be using the term "window function" in a slightly different manner than in more classical time series analysis discussions. Instead of describing a traditional window function, such as the Hann window, we take an approach similar to that of VanderPlas (2018) where the window function describes how the light curve was sampled in time. This window function has predictable effects on the LS periodograms

Table 2.3: A description of the data for the detected Lomb-Scargle failure modes , available in a machine-readable format online.

| Name | Table Header | Units | Description |
|---|---|---|---|
| *Gaia* Source ID | `gaiaid` | – | *Gaia* EDR3 `source_id` |
| False Alarm Probability | `fap` | – | The estimated false alarm probability of the rotation period |
| Rotation Period ($P_{\rm rot}$) | `prot` | d | The measured rotation period of the star |
| Half Period Alias | `m=2` | d | $m = 2$, and $n = 0$ |
| Third Period Alias | `m=3` | d | $m = 3$, and $n = 0$ |
| First Month Failure Mode | `monthn=-2` | d | $m = 1$, $n = -2$, and $\delta P \approx 29.5$ Days |
| Second Month Failure Mode | `monthn=-1` | d | $m = 1$, $n = -1$, and $\delta P \approx 29.5$ Days |
| Third Month Failure Mode | `monthn=+1` | d | $m = 1$, $n = 1$, and $\delta P \approx 29.5$ Days |
| Fourth Month Failure Mode | `monthn=+2` | d | $m = 1$, $n = 2$, and $\delta P \approx 29.5$ Days |
| First Year Failure Mode | `yearn=-2` | d | $m = 1$, $n = -2$, and $\delta P \approx 380.8$ Days |
| Second Year Failure Mode | `yearn=-1` | d | $m = 1$, $n = -1$, and $\delta P \approx 380.8$ Days |
| Third Year Failure Mode | `yearn=+1` | d | $m = 1$, $n = 1$, and $\delta P \approx 380.8$ Days |
| Fourth Year Failure Mode | `yearn=+2` | d | $m = 1$, $n = 2$, and $\delta P \approx 380.8$ Days |

All alias and failure mode values are the output of Eq. 2.9 with $P_{\rm true} = P_{\rm rot}$ and are only included in the table if a peak was detected at that period in the periodogram.

computed from the data, which can all be combined into one equation (Eq. 47 in VanderPlas 2018):

$$P_{\rm obs} = \left| \frac{m}{P_{\rm true}} + \frac{n}{\delta P} \right|^{-1}, \tag{2.9}$$

where $P_{\rm obs}$ is the observed peak in the periodogram, $P_{\rm true}$ is the true period of the underlying signal, and $m$ and $n$ are integers. $m = 1$ and $n = 0$ yields the true period, and $m = 2$ and $n = 0$ represents the classic case of half-period aliasing, however they can both take any integer value, positive or negative. The final term, $\delta P$, is the period of a peak in the window function's periodogram; there are typically more than one, and for our CFHT observations there were two dominant ones. They were the "month window peak" ($\delta P \approx 29.5$ Days) arising from only observing during the bright lunar phases, and the "year window peak" ($\delta P \approx 380.8$ Days) arising from only observing when the cluster is up. The exact values of each depends on the precise sampling in time (i.e., on the completeness of the light curve). The effects of these window peaks can be easily seen in a scatter plot of $P_{\rm true}$ vs $P_{\rm obs}$, which we have plotted using the results of a complete set of injections into one of our CFHT light curves (Fig. 2.12). There is no way to determine if the period of maximum power in a periodogram corresponds to $P_{\rm true}$ or one of its failure modes, $P_{\rm obs}$, with absolute certainty. Moreover, because $m$ and $n$ are integers there is no continuum of window effects, meaning a standard deviation computed across the peaks in a periodogram is a poor description of the uncertainty. VanderPlas (2018) provide a prescription for how one can use detected failure modes to improve the accuracy of interpreting periodgrams. We did not use their prescription, instead we found that many of the stars identified as likely to be failure modes as opposed to true rotation periods by their method are rejected in our iterative-outlier rejection and thus already excluded from our analysis. We have included a table of all the detected potential failure modes associated with each of our reported $P_{\rm rot}$ values in Table 2.3. Readers who are interested in further trimming to create their own subset of the M67 rotation periods reported here may use these values in a prescription like that of Sec. 7.2 of VanderPlas (2018).

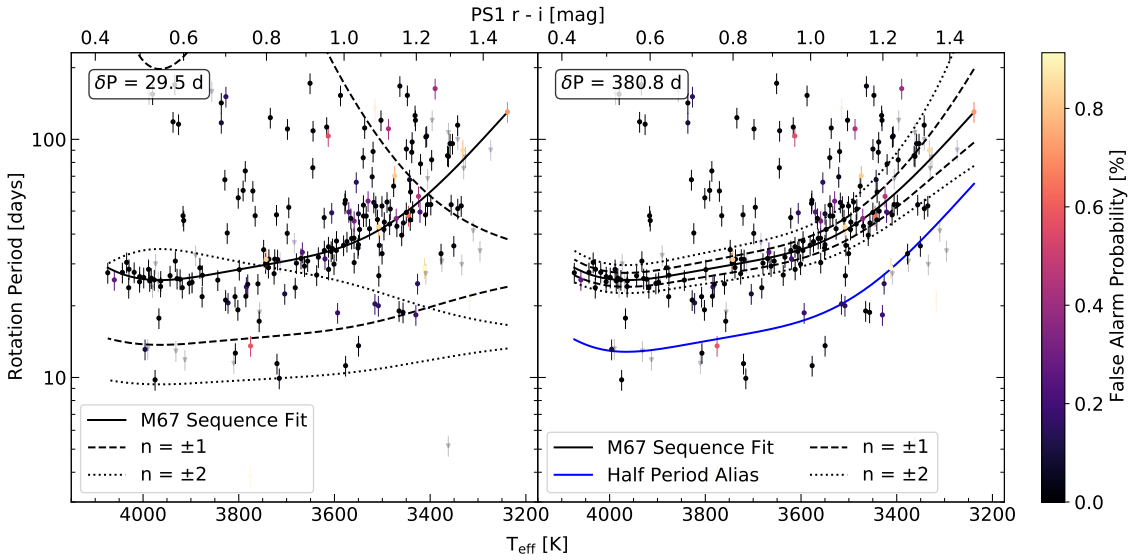


Figure 2.13: **Both Panels**: The rotation period vs effective temperature of M67 members with our fit to the M67 sequence (solid black). Dashed lines are the result of assuming our fit to the sequence is the true period in Eq. 2.9 along with $m = 1$ and $n = \pm 1$. Dotted lines are the same, but with $n = \pm 2$. **Left Panel**: Using 29.5 Days for $\delta P$ Eq. 2.9. **Right Panel**: Using 380.8 Days for $\delta P$ Eq. 2.9. Additionally the half-period alias of Eq. 2.7 is in solid blue.

### 2.5.2 Deviations from the Sequence

There are a number of mechanisms that can result in an incorrectly measured value of $P_{\rm rot}$, both observational and astrophysical. Astrophysically, spot pattern evolution can spread the power from a rotation signal into multiple peaks in the periodogram, as well as shift the central location of these peaks. By using *Kepler* light curves as a part of our injection and recovery tests (Sec. 2.4.1) we are able to quantify the effect this has on our recovery. Comparing the bins with majority *Kepler* light curves to their neighbors with majority synthetic light curves in Fig. 2.9 indicates that spot pattern evolution among the *Kepler* light curves lead to a ∼15-20% drop in recovery. The same comparison using Fig. 2.10 shows an equivalent uptick in false positives, highlighting the impact of spreading the power across multiple peaks in the periodogram. Additionally, Basri & Nguyen (2018) have shown that stars with lower $T_{\rm eff}$ and longer $P_{\rm rot}$ tend to favor a "double dip" spot pattern that lends itself to half-period aliasing. However, the results of our injection and recovery

tests suggest this is a relatively minor effect for our data set (see the half period alias line in Fig. 2.12). Finally, close binary systems will have rotation periods that appear as outliers in the data. Such systems are affected both by the confusion of brightness modulations in both stars as well as tidal forces changing their rotational evolution relative to single stars. We have mitigated the contamination from binary stars through our CMD cuts (Sec. 2.3.1). Observationally, we were also limited by our irregular sampling in time, such effects are described by the Lomb-Scargle failure modes (see Sec. 2.5.1). This means that even a perfectly stable sinusoid can be recovered incorrectly as the signal-to-noise ratio on the data decreases. With these effects in mind we believe that the use of iterative outlier rejection for our reported fit to the $T_{\rm eff}$ vs $P_{\rm rot}$ sequence was justified.

To demonstrate this, we substituted Eq. 2.7 for $P_{\rm true}$ in Eq. 2.9, and plotted the resulting sequences alongside our original results in Fig. 2.13. Given the difference in the effect of each window peak we plotted the month and year effects separately. For the collection of stars rotating faster than our fit to the $T_{\rm eff}$ vs $P_{\rm rot}$ sequence, they align well with two possible cases: 1) they fall along the half period alias of our fit, or 2) they fall along a sequence that is associated with the month window peak (left panel of Fig. 2.13). The sequences associated with the year window peak show that these failure modes contribute to the scatter about our fit to the sequence. This, combined with the precision on our $P_{\rm rot}$ values derived from the injection and recovery tests (Fig. 2.8), are what prevent us from measuring a $T_{\rm eff}$ vs $P_{\rm rot}$ sequence that is as sharply defined as the slow rotator sequences observed in younger clusters (e.g., Praespe and NGC 6811; Douglas et al. 2017, 2019; Curtis et al. 2019).

Finally, there remain a number of stars with relatively long rotation periods ($P_{\rm rot} \gtrsim 40$ d) and high temperatures ($T_{\rm eff} \gtrsim 3600$ K) that are inconsistent with our fitted sequence and its expected failure modes. To gain some insight into the origin of these inconsistent stars we binned our $P_{\rm rot}$ values and computed the fraction of stars in a period bin that were inconsistent with the fitted sequence. Then we estimated the $S_{\rm ph}$ values for these stars, allowing us to compare the computed fractions to the false positive rates of Fig.

2.10. The stars inconsistent with the sequence have a mean $S_{\rm ph}$ of 0.3% with a standard deviation of 0.2%, compared to a mean $S_{\rm ph}$ of 0.4% with a standard deviation of 0.1% for the stars of equivalent temperature consistent with the sequence. Given these $S_{\rm ph}$ values, the inconsistency fractions of $20-50\%$ align well with the false positive rates. Moreover, the inconsistent stars all have detected failure modes that are consistent with the fitted sequence itself, whereas those on the sequence primarily have detected failure modes consistent with a half-period alias. A multi-term model would aid in clarifying the true rotation period of these stars, however the sparse sampling in our data made those fits poorly conditioned. Therefore we are satisfied with their exclusion from our fit to the sequence. We postulate that these stars were affected by either spot pattern evolution or the signal-to-noise ratio of the data, both of which contribute to how likely a failure mode is to be recovered instead of the true rotation period. Confirmation would require follow-up observations at much higher cadence and with more regular sampling in time.

## 2.6 Discussion

We first compared our observations (the 64 stars our iterative outlier rejection converged to, Sec. 2.5) against the predictions of two classes of gyrochronological models: empirical and theoretical (Fig. 2.14). Empirical models are agnostic to the physics of magnetic breaking and anguluar momentum transport, fitting a relation to a set of periods and ages often as a function of color. Generally they follow a Skumanich-like relation of $P_{\rm rot} \propto t^n$, using cluster data and the Sun as anchor points to tune the value of the exponent. On the other hand, theoretical models make assumptions regarding the underlying physics and spin-down that manifests from their description. Whether they are empirical or theoretical in nature, all models are calibrated against objects of known age and rotation period, relatively few of which are young M dwarfs, meaning that their predictions for the age of M67 are an extrapolation.

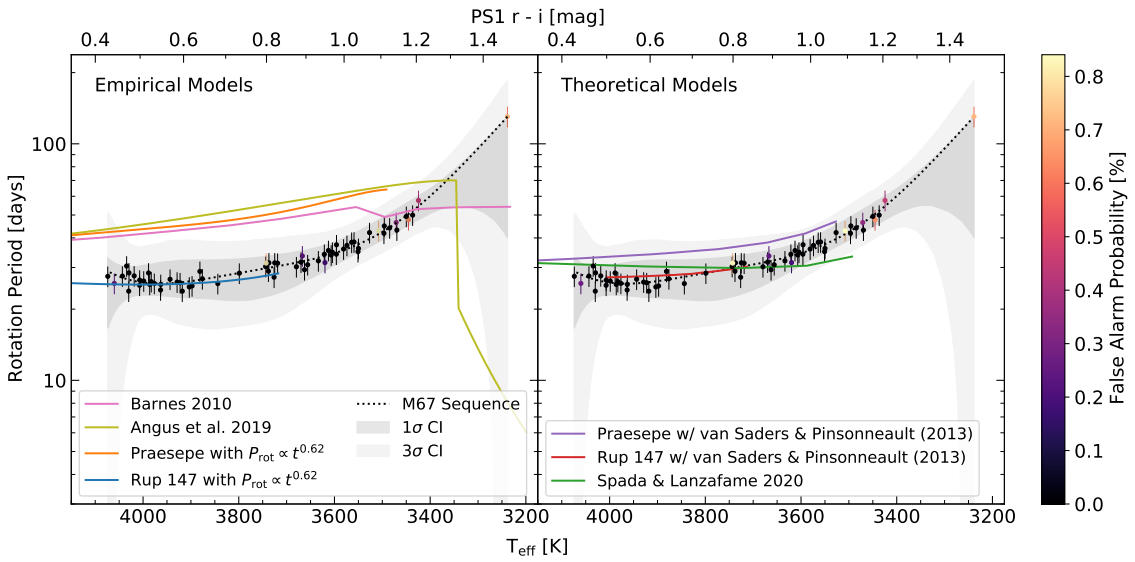


Figure 2.14: **Left Panel**: The selected subset (from iterative outlier rejection, Sec. 2.5) of M67 rotation periods versus their effective temperatures. The shaded region in gray is the confidence interval of the fit, plotted as a dotted black line. Predictions for the sequence from the empirical models are plotted as colored lines. **Right Panel**: The same as the left panel, but with predictions from the theoretical models.

There are four empirical relations included in our comparison. First is the Barnes (2010) model, where $dP_{\rm rot}/dt$ is parameterized in terms of the Rossby number ($Ro$) and two dimensionless constants calibrated on the Sun and young open cluster observations. Second, the Angus et al. (2019) empirical relation, which is a broken power law with mass fit to the sequence of Praesepe and a spin-down law tuned to replicate the Sun. Finally, we evolved the sequences of Praesepe (670 Myr; Douglas et al. 2017, 2019) and Ruprecht 147 (2.7 Gyr; Curtis et al. 2020) forward in time through the use of a simple Skumanich-like spin down: $P_{\rm rot}(4\ {\rm Gyr}) = P_{\rm rot,0}(4\ {\rm Gyr}/t_0)^{0.62}$. For the hotter stars in our sample all of these empirical relations, with one exception, predict that the stars of M67 should be rotating $\sim$ 10-20 days slower than observed. The exception is the Skumanich-like spin down relation launched from the stars of Ruprecht 147, which provides an excellent match to our data for the earlier M dwarfs ($T_{\rm eff} \gtrsim 3700$ K), for the later M dwarfs there were no data available in Ruprecht 147.

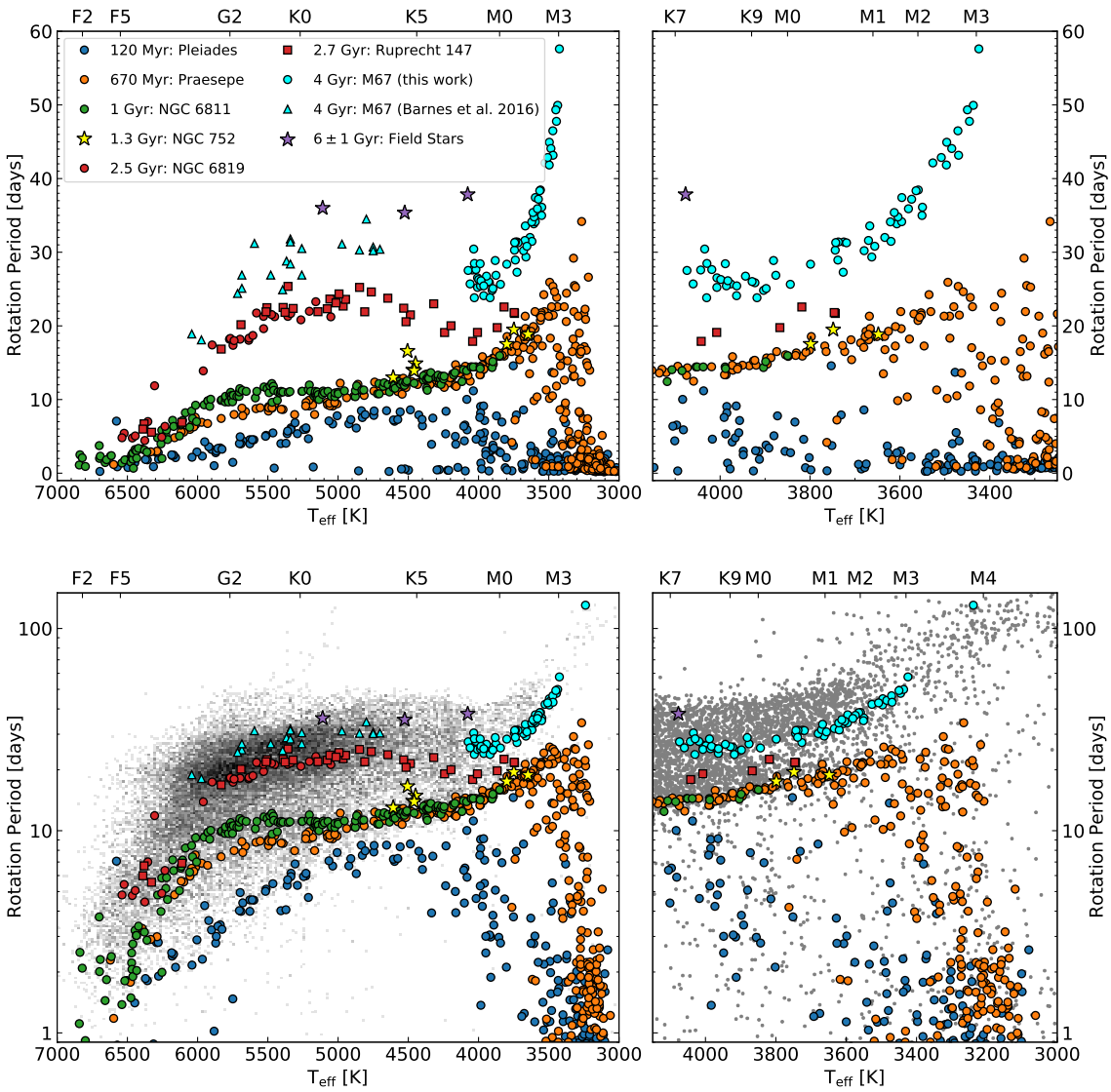


Figure 2.15: **Top Left Panel**: A replication of the first panel of Fig. 7 of Curtis et al. (2020), but with our results and the results of Barnes et al. (2016) added. **Top Right Panel**: A Subset of the left panel, zoomed in on the $T_{\rm eff}$ range of the results presented in this paper.**Bottom Left Panel**: Same as top left panel, but now plotted over a 2D histogram of field star rotation periods. **Bottom Right Panel**: Same as top right panel, but now plotted over field star rotation periods. In all cases, the colored points are a collection of open clusters which have been used as gyrochronological benchmarks. Benchmarks include the Pleiades (120 Myr; Rebull et al. 2016), Praesepe (670 Myr; Douglas et al. 2017, 2019), NGC 6811 (1 Gyr; Curtis et al. 2019), NGC 752 (1.4 Gyr; Agüeros et al. 2018), NGC 6819/Ruprecht 147 (2.5 Gyr projected forward by Curtis et al./2.7 Gyr; Meibom et al. 2015; Curtis et al. 2020), M67 (4 Gyr; Barnes et al. 2016, and this work), and three field stars: $\alpha$ Cen B and 61 Cyg A and B (Table 3 of Curtis et al. 2020, and references therein). Field stars are taken from a collection of literature sources: *Kepler* (Santos et al. 2019), the PS1 Medium Deep Survey (Kado-Fong et al. 2016), MEarth (Newton et al. 2016, 2018), CARMENES (Díez Alonso et al. 2019), Evryscope (Howard et al. 2020), and the K2SDSS sample (Popinchalk et al. 2021).

The first of the two theoretical models we considered is from van Saders & Pinsonneault (2013) and described therein. Similar to our Skumanich-like empirical relation, we launched this model from two starting places: Praesepe and Ruprecht 147. This model is calibrated to match the spin down of solar mass stars and the Sun, and then applied to our low-mass M67 members. Braking laws of this form perform well on the Sun but fail to capture the rotational evolution during the first few hundreds of Myrs in young clusters (see Douglas et al. 2017; Breimann et al. 2021; Roquette et al. 2021); it is unclear to what degree the issue is with the braking law itself (saturation, core envelope decoupling, etc.) or with the assumed distribution of initial rotation periods (Roquette et al. 2021). We manage these early-time uncertainties by starting our models as solid body rotators at Praesepe age and rotation rate, and evolving them forward to M67. The model evolved forward from Praesepe is a better match than the empirical relations, as it is within the $3\sigma$ confidence interval, but still predicts that the stars of M67 should be rotating slower than we observed. The model evolved forward from Ruprecht 147 provides an excellent match, being very closely aligned with the empirical relation launched from the same starting point, although this is again limited by a lack of later M dwarfs in the Ruprecht 147 data.

The second theoretical model we included is the model of Spada & Lanzafame (2020). This iteration on the model includes some minor adjustments from that of Lanzafame & Spada (2015), a core-envelope decoupling model. Their model incorporates a mass-dependent wind-braking law that follows the classical rotation rate dependence of Kawaler (1988), $\frac{dJ}{dt} \propto \omega^3$. It also uses a two-zone approach to the interior, treating the core and envelope as two separate rotationally solid bodies that are allowed to exchange angular momentum. As a result, this model explains the apparent stalling of spin-down as a epoch during which significant angular momentum transport occurs from the core to the envelope, balancing out the angular momentum the envelope loses to wind-braking. The prediction of this model agrees with the observations quite well down to a $T_{\rm eff}$ of around 3600 K. At this point, the model's prediction is too fast compared to our observations, though still consistent at the $3\sigma$ level.

In total, we have found three models that provide an excellent (i.e., within $1\sigma$) match to our observations of M67. Of these models, two are solid body spin-down (one theoretical, one empirical) applied to the stars of Ruprecht 147, which we interpret as a sign that the late stages of low-mass stellar spin-down are dominated by solid body rotation. The other model is that of Spada & Lanzafame (2020), which is both the only core-envelope decoupling model tested, as well as the only model launched from the birth of the star. The excellent agreement between it and our observations makes a compelling case for the core-envelope decoupling theory.

### 2.6.1 The Case for Core-Envelope Decoupling

The evidence for core-envelope decoupling goes deeper than the agreement between the model of Spada & Lanzafame (2020) and our observations. In the core-envelope decoupling framework, after the epoch of significant angular momentum transport occurs, the expectation is that the core and envelope of the star have equalized in angular velocity. At this point, the star spins down as a solid body. If the stars of Ruprecht 147 have resumed their spin-down (Curtis et al. 2020), core-envelope decoupling would predict that they are now spinning down as solid bodies. The precise agreement between our solid body and empirical models launched from Ruprecht 147 and our observations implies that this is the case, at least through the age of M67.

Another important test of core-envelope decoupling lies in the behavior of spin-down for stars that are nearly or fully convective. The diminishing size of the core limits the amount of angular momentum it can store relative to the envelope, reducing the length of time the star's spin-down would stall. Furthermore, stars with no radiative core should not stall their spin-down at all. Curtis et al. (2020) provide an empirical relation for the age at which stars resume spinning down. They find:

$$t_{\rm R} = 0.202 \text{ Gyr} \times \left( \frac{T_{\rm eff}}{5770 \text{ K}} \right)^{-5.11}, \tag{2.10}$$

based on a simplified model where spin-down comes to a full stop and then suddenly resumes after a mass-dependent length of time. If we extrapolate this relation to later spectral types (i.e., beyond M0), we find that by M1.5 the age at which spin down resumes is approaching that of M67 (3.6 Gyr vs 4 Gyr), and by M2 this age has potentially exceeded that of M67 (4.6 Gyr). However, the stars in this range of temperatures (M1-M3) are rotating ∼10-30 days slower than their younger counterparts (top two panels of Fig. 2.15), implying they have been spinning-down for at least part of the intervening ∼ 3 Gyrs. This is suggestive of a need for a $t_{\rm R}$ relation that has a turnover as it approaches the fully convective boundary, as expected in the core-envelope decoupling framework. Observations of younger M dwarfs of these spectral types (e.g., those in Ruprecht 147 or NGC 752) will be a critical test for determining when these stars resumed their spin-down.

### 2.6.2 M67 and the Field

We have also compared our observations to an ensemble of field star rotation periods collected from a variety of sources. The largest contributor to this collection is the *Kepler* sample, with temperatures and rotation periods from Santos et al. (2019). The rest are predominantly M dwarfs with rotation periods from: the PS1 Medium Deep Survey (Kado-Fong et al. 2016), MEarth (Newton et al. 2016, 2018), CARMENES (Díez Alonso et al. 2019), Evryscope (Howard et al. 2020), and the K2SDSS sample (Popinchalk et al. 2021). Popinchalk et al. (2021) provided the *Gaia* DR2 identifiers for the targets from all of these surveys, which we used to obtain temperatures from v8 of the *TESS* Input Catalog (TIC) (Stassun et al. 2019). We then plotted these field stars with the open cluster data (bottom two panels of Fig. 2.15), ignoring any stars which did not have a temperature in TIC.

Field M dwarfs follow a bimodality in their rotation periods (Kado-Fong et al. 2016; Newton et al. 2016; Howard et al. 2020). Using kinematic ages, Newton et al. (2016) speculated that the transition between the fast and slow populations must be quick, and must occur between the ages of 2 and 5 Gyr. The stars of M67 fall along the lower envelope of the slow rotator population, suggesting that they represent convergence onto a slow

rotator sequence for M dwarfs. The age of M67 (4 Gyr) is consistent with the bounds for the transition. Higher cadence observations are needed to confirm whether or not there are still rapid rotators in M67, a lack of which would make M67 a fully converged slow rotator sequence. Since accurate gyrochronology depends on stars converging to a slow rotator sequence, the age of M67 serves as a lower bound for accurate gyrochronological ages of M dwarfs.

Another interesting feature seen in the distribution of field star rotation periods is the intermediate period gap. This is a bimodal distribution of stars with $T_{\rm eff}$ values less than 5000 K and intermediate rotation periods (15-25 Days, McQuillan et al. 2013). A number of explanations have been put forth to explain this gap, including a lull in star-formation (Davenport 2017), a transition to faculae-dominated photospheres (Reinhold et al. 2019), or an epoch of accelerated spin-down during the recoupling of the core and envelope (McQuillan et al. 2013; Gordon et al. 2021). Open cluster data shows that any explanation relying on the gap stars having a common age is incorrect (Curtis et al. 2020). Instead the mechanism that causes this gap must occur at different times for stars of different masses. The stars of M67 appear along the upper envelope of the intermediate period gap, suggesting an upper bound of 4 Gyr for the age by which this mechanism has occurred. Furthermore, if the gap is indeed caused by accelerated spin-down during core-envelope recoupling, then the stars along the upper envelope of the intermediate period gap should be composed of stars that are spinning down as solid bodies, in line with our observations.

### 2.6.3 Evidence of a Unique Spin-Down History

While this description is compelling, some caution is important. Somers & Pinsonneault (2016) identified M67 as an outlier among open clusters in terms of its lithium abundance. Having demonstrated that Li depletion is a strong test of core-envelope recoupling they concluded that the most likely scenario explaining M67's Li abundances is an "intrinsically different mixing history" driven by a surplus of rapid rotators in the cluster's early years. Observations of young clusters and associations show that massive stars in large clusters

can drive photoevaporation of the disks of nearby lower mass stars, shortening disk lifetimes and resulting in a larger population of rapid rotators (Roquette et al. 2021). Such a surplus of rapid rotators would shift the mean sequence of M67 to faster rotation periods compared to stars of equivalent ages until the initial conditions are forgotten. However, this will not affect the braking laws describing their spin-down. We can control for M67's unique initial rotation periods by modeling a variety of cases for the initial conditions, as well as observing other clusters of similar ages.

## 2.7 Conclusions

In this paper we have:

- Generated a new catalog of 1807 M67 members based on *Gaia* EDR3 parallaxes and proper motions, identified potential unresolved binaries by their location on the cluster's CMD, and calculated the color-based effective temperatures for the late K and early M dwarf single members of M67.

- Reported the rotation periods for 294 of these M67 members, providing a sample of 4 Gyr old late K and early M dwarfs for calibrating gyrochronological models and a polynomial fit to the sequence they form in $T_{\rm eff}$ vs $P_{\rm rot}$ for use as a gyrochrone:

$$P_{\rm rot}(T_{\rm eff,4K}) = 9.66 \times 10^{-10} \cdot T_{\rm eff,4K}^4 + 8.25 \times 10^{-7} \cdot T_{\rm eff,4K}^3 + 2.69 \times 10^{-4} \cdot T_{\rm eff,4K}^2 + 0.016 \cdot T_{\rm eff,4K} + 25.9,$$

  or

$$P_{\rm rot}(r-i) = 292 \cdot (r-i)^4 - 895 \cdot (r-i)^3 + 1054 \cdot (r-i)^2 - 543 \cdot (r-i) + 127.9, \quad (2.11)$$

- Having compared the gyrochronological models to our gyrochrone, we found that late K and early M dwarfs spin down as solid bodies between 2.7 and 4 Gyr of age.

This behavior is broadly consistent with core-envelope decoupling models of stellar spin-down.

RD would like to acknowledge the organizers of the Fifty Years of the Skumanich Relation conference for facilitating some enlightening discussions around these data, especially those with Jason Curtis. RD, JvS, and EG acknowledge support from NSF Astronomy & Astrophysics grant AST-1817215. ARGS acknowledges the support from the FCT and FEDER/COMPETE2020 through work contract No. 2020.02480.CEECIND/CP1631/CT0001 and grants UIDP/04434/2020; PTDC/FIS-AST/30389/2017 & POCI-01-0145-FEDER-030389. R.A.G. acknowledges the support from PLATO CNES grant. S.M. acknowledges support by the Spanish Ministry of Science and Innovation with the Ramon y Cajal fellowship number RYC-2015-17697 and the grant number PID2019-107187GB-I00. Based on observations obtained with MegaPrime/MegaCam, a joint project of CFHT and CEA/DAPNIA, at the Canada-France-Hawaii Telescope (CFHT) which is operated by the National Research Council (NRC) of Canada, the Institut National des Science de l'Univers of the Centre National de la Recherche Scientifique (CNRS) of France, and the University of Hawaii. The observations at the Canada-France-Hawaii Telescope were performed with care and respect from the summit of Maunakea which is a significant cultural and historic site. The Pan-STARRS1 Surveys (PS1) and the PS1 public science archive have been made possible through contributions by the Institute for Astronomy, the University of Hawaii, the Pan-STARRS Project Office, the Max-Planck Society and its participating institutes, the Max Planck Institute for Astronomy, Heidelberg and the Max Planck Institute for Extraterrestrial Physics, Garching, The Johns Hopkins University, Durham University, the University of Edinburgh, the Queen's University Belfast, the Harvard-Smithsonian Center for Astrophysics, the Las Cumbres Observatory Global Telescope Network Incorporated, the National Central University of Taiwan, the Space Telescope Science Institute, the National Aeronautics and Space Administration under Grant No. NNX08AR22G issued through the Planetary Science Division of the NASA Science Mission Directorate, the National Science Foundation Grant

No. AST-1238877, the University of Maryland, Eotvos Lorand University (ELTE), the Los Alamos National Laboratory, and the Gordon and Betty Moore Foundation.

## 2.8 Example Light Curves and Periodograms

A light curve, phase-folded light curve, and periodogram are available for every star in Table 2.2, included here are two examples. The full set is available in the online journal.

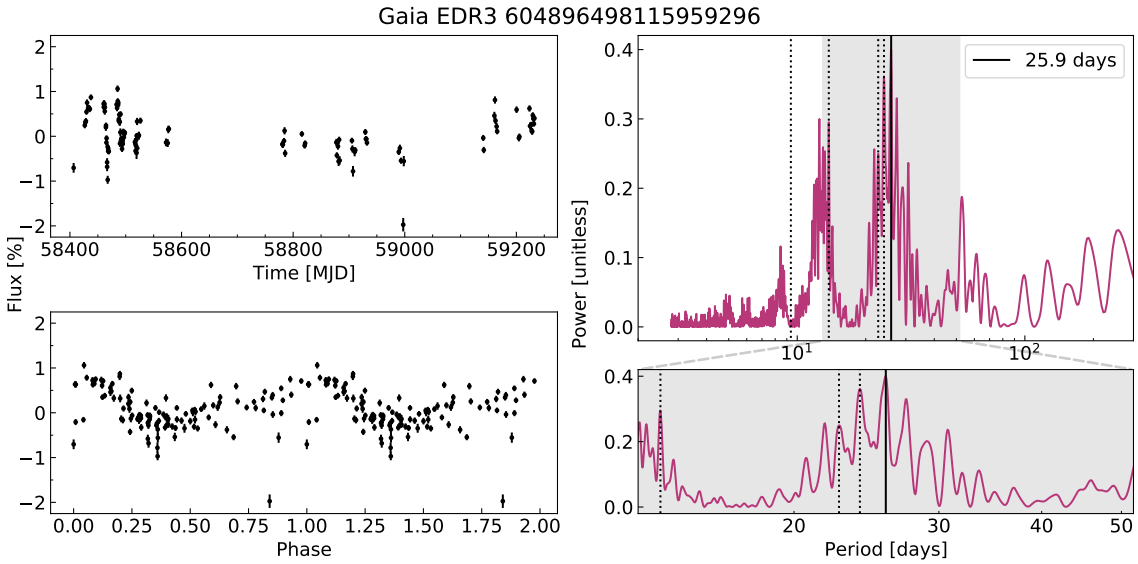


(a)

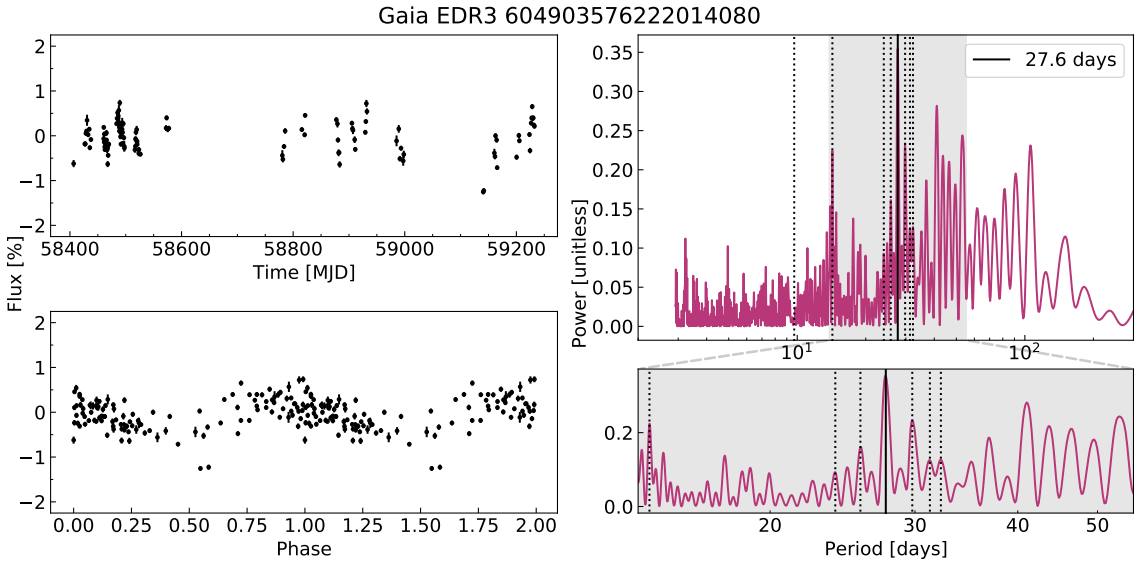


(b)

Figure 2.16: Example light curves and periodograms for select cluster members. In the top left of each target's set is the light curve of the target. Bottom left is the phase-folded version, folded on the period of max power in the periodogram. On the right, the periodogram and a subset centered on the period of max power. Window peaks are denoted with vertical dotted lines. The complete figure set (594 images) is available in the online journal.

# References


Agüeros, M. A., Bowsher, E. C., Bochanski, J. J., Cargile, P. A., Covey, K. R., Douglas, S. T., Kraus, A., Kundert, A., Law, N. M., Ahmadi, A., & Arce, H. G. 2018, ApJ, 862, 33

Allain, S. 1998, A&A, 333, 629

Angus, R., Aigrain, S., Foreman-Mackey, D., & McQuillan, A. 2015, MNRAS, 450, 1787

Angus, R., Morton, T. D., Foreman-Mackey, D., van Saders, J., Curtis, J., Kane, S. R., Bedell, M., Kiman, R., Hogg, D. W., & Brewer, J. 2019, AJ, 158, 173

Aumer, M. & Binney, J. J. 2009, MNRAS, 397, 1286

Balaguer-Núñez, L., Galadí-Enríquez, D., & Jordi, C. 2007, A&A, 470, 585

Baluev, R. V. 2008, MNRAS, 385, 1279

Barnes, S. A. 2003, ApJ, 586, L145

—. 2007, ApJ, 669, 1167

—. 2010, ApJ, 722, 222

Barnes, S. A., Weingrill, J., Fritzewski, D., Strassmeier, K. G., & Platais, I. 2016, ApJ, 823, 16

Basri, G. & Nguyen, H. T. 2018, ApJ, 863, 190

Belokurov, V., Penoyre, Z., Oh, S., Iorio, G., Hodgkin, S., Evans, N. W., Everall, A., Koposov, S. E., Tout, C. A., Izzard, R., Clarke, C. J., & Brown, A. G. A. 2020, MNRAS, 496, 1922

Berdinas, Z. M., Rodriguez-Lopez, C., Amado, P. J., Anglada-Escude, G., Barnes, J. R., MacDonald, J., Zechmeister, M., & Sarmiento, L. F. 2017, MNRAS, 469, 4268

Bildsten, L., Brown, E. F., Matzner, C. D., & Ushomirsky, G. 1997, ApJ, 482, 442

Bochanski, J. J., Hawley, S. L., Covey, K. R., West, A. A., Reid, I. N., Golimowski, D. A., & Ivezić, Ž. 2010, AJ, 139, 2679

Boulade, O., Charlot, X., Abbon, P., Aune, S., Borgeaud, P., Carton, P.-H., Carty, M., Da Costa, J., Deschamps, H., Desforge, D., Eppellé, D., Gallais, P., Gosset, L., Granelli, R., Gros, M., de Kat, J., Loiseau, D., Ritou, J. ., Roussé, J. Y., Starzynski, P., Vignal, N., & Vigroux, L. G. 2003, in Society of Photo-Optical Instrumentation Engineers (SPIE) Conference Series, Vol. 4841, Instrument Design and Performance for Optical/Infrared Ground-based Telescopes, ed. M. Iye & A. F. M. Moorwood, 72–81

Bradley, L., Sipőcz, B., Robitaille, T., Tollerud, E., Vinícius, Z., Deil, C., Barbary, K., Wilson, T. J., Busko, I., Günther, H. M., Cara, M., Conseil, S., Bostroem, A., Droettboom, M., Bray, E. M., Bratholm, L. A., Lim, P. L., Barentsen, G., Craig, M., Pascual, S., Perren, G., Greco, J., Donath, A., de Val-Borro, M., Kerzendorf, W., Bach, Y. P., Weaver, B. A., D'Eugenio, F., Souchereau, H., & Ferreira, L. 2020, astropy/photutils: 1.0.0

Breimann, A. A., Matt, S. P., & Naylor, T. 2021, ApJ, 913, 75

Carraro, G. & Chiosi, C. 1994, A&A, 288, 751

Chaplin, W. J., Bedding, T. R., Bonanno, A., Broomhall, A. M., García, R. A., Hekker, S., Huber, D., Verner, G. A., Basu, S., Elsworth, Y., Houdek, G., Mathur, S., Mosser, B., New, R., Stevens, I. R., Appourchaux, T., Karoff, C., Metcalfe, T. S., Molenda-Żakowicz,

J., Monteiro, M. J. P. F. G., Thompson, M. J., Christensen-Dalsgaard, J., Gilliland, R. L., Kawaler, S. D., Kjeldsen, H., Ballot, J., Benomar, O., Corsaro, E., Campante, T. L., Gaulme, P., Hale, S. J., Handberg, R., Jarvis, E., Régulo, C., Roxburgh, I. W., Salabert, D., Stello, D., Mullally, F., Li, J., & Wohler, W. 2011, ApJ, 732, L5

Curtis, J. L., Agüeros, M. A., Douglas, S. T., & Meibom, S. 2019, ApJ, 879, 49

Curtis, J. L., Agüeros, M. A., Matt, S. P., Covey, K. R., Douglas, S. T., Angus, R., Saar, S. H., Cody, A. M., Vanderburg, A., Law, N. M., Kraus, A. L., Latham, D. W., Baranec, C., Riddle, R., Ziegler, C., Lund, M. N., Torres, G., Meibom, S., Aguirre, V. S., & Wright, J. T. 2020, ApJ, 904, 140

Davenport, J. R. A. 2017, ApJ, 835, 16

Deacon, N. R. & Kraus, A. L. 2020, MNRAS, 496, 5176

Demarque, P., Green, E. M., & Guenther, D. B. 1992, AJ, 103, 151

Denissenkov, P. A., Pinsonneault, M., Terndrup, D. M., & Newsham, G. 2010, ApJ, 716, 1269

Díez Alonso, E., Caballero, J. A., Montes, D., de Cos Juez, F. J., Dreizler, S., Dubois, F., Jeffers, S. V., Lalitha, S., Naves, R., Reiners, A., Ribas, I., Vanaverbeke, S., Amado, P. J., Béjar, V. J. S., Cortés-Contreras, M., Herrero, E., Hidalgo, D., Kürster, M., Logie, L., Quirrenbach, A., Rau, S., Seifert, W., Schöfer, P., & Tal-Or, L. 2019, A&A, 621, A126

Douglas, S. T., Agüeros, M. A., Covey, K. R., & Kraus, A. 2017, ApJ, 842, 83

Douglas, S. T., Curtis, J. L., Agüeros, M. A., Cargile, P. A., Brewer, J. M., Meibom, S., & Jansen, T. 2019, ApJ, 879, 100

Dressing, C. D. & Charbonneau, D. 2015, ApJ, 807, 45

Duchêne, G. & Kraus, A. 2013, ARA&A, 51, 269

Epstein, C. R. & Pinsonneault, M. H. 2014, ApJ, 780, 159

Fan, X., Burstein, D., Chen, J. S., Zhu, J., Jiang, Z., Wu, H., Yan, H., Zheng, Z., Zhou, X., Fang, L. Z., Chen, F., Deng, Z., Chu, Y., Hester, J. J., Windhorst, R. A., Li, Y., Lu, P., Sun, W. H., Chen, W. P., Tsay, W. S., Chiueh, T. H., Chou, C. K., Ko, C. M., Lin, T. C., Guo, H. J., & Byun, Y. I. 1996, AJ, 112, 628

Flewelling, H. A., Magnier, E. A., Chambers, K. C., Heasley, J. N., Holmberg, C., Huber, M. E., Sweeney, W., Waters, C. Z., Calamida, A., Casertano, S., Chen, X., Farrow, D., Hasinger, G., Henderson, R., Long, K. S., Metcalfe, N., Narayan, G., Nieto-Santisteban, M. A., Norberg, P., Rest, A., Saglia, R. P., Szalay, A., Thakar, A. R., Tonry, J. L., Valenti, J., Werner, S., White, R., Denneau, L., Draper, P. W., Hodapp, K. W., Jedicke, R., Kaiser, N., Kudritzki, R. P., Price, P. A., Wainscoat, R. J., Chastel, S., McLean, B., Postman, M., & Shiao, B. 2020, ApJS, 251, 7

Gaia Collaboration, Brown, A. G. A., Vallenari, A., Prusti, T., de Bruijne, J. H. J., Babusiaux, C., Biermann, M., Creevey, O. L., Evans, D. W., Eyer, L., Hutton, A., Jansen, F., Jordi, C., Klioner, S. A., Lammers, U., Lindegren, L., Luri, X., Mignard, F., Panem, C., Pourbaix, D., Randich, S., Sartoretti, P., Soubiran, C., Walton, N. A., Arenou, F., Bailer-Jones, C. A. L., Bastian, U., Cropper, M., Drimmel, R., Katz, D., Lattanzi, M. G., van Leeuwen, F., Bakker, J., Cacciari, C., Castañeda, J., De Angeli, F., Ducourant, C., Fabricius, C., Fouesneau, M., Frémat, Y., Guerra, R., Guerrier, A., Guiraud, J., Jean-Antoine Piccolo, A., Masana, E., Messineo, R., Mowlavi, N., Nicolas, C., Nienartowicz, K., Pailler, F., Panuzzo, P., Riclet, F., Roux, W., Seabroke, G. M., Sordo, R., Tanga, P., Thévenin, F., Gracia-Abril, G., Portell, J., Teyssier, D., Altmann, M., Andrae, R., Bellas-Velidis, I., Benson, K., Berthier, J., Blomme, R., Brugaletta, E., Burgess, P. W., Busso, G., Carry, B., Cellino, A., Cheek, N., Clementini, G., Damerdji, Y., Davidson, M., Delchambre, L., Dell'Oro, A., Fernández-Hernández, J., Galluccio, L., García-Lario, P., Garcia-Reinaldos, M., González-Núñez, J., Gosset, E., Haigron, R., Halbwachs, J. L., Hambly, N. C., Harrison, D. L., Hatzidimitriou, D., Heiter, U., Hernández, J., Hestroffer, D., Hodgkin, S. T., Holl, B., Janßen, K., Jevardat de Fombelle,

G., Jordan, S., Krone-Martins, A., Lanzafame, A. C., Löffler, W., Lorca, A., Manteiga, M., Marchal, O., Marrese, P. M., Moitinho, A., Mora, A., Muinonen, K., Osborne, P., Pancino, E., Pauwels, T., Petit, J. M., Recio-Blanco, A., Richards, P. J., Riello, M., Rimoldini, L., Robin, A. C., Roegiers, T., Rybizki, J., Sarro, L. M., Siopis, C., Smith, M., Sozzetti, A., Ulla, A., Utrilla, E., van Leeuwen, M., van Reeven, W., Abbas, U., Abreu Aramburu, A., Accart, S., Aerts, C., Aguado, J. J., Ajaj, M., Altavilla, G., Álvarez, M. A., Álvarez Cid-Fuentes, J., Alves, J., Anderson, R. I., Anglada Varela, E., Antoja, T., Audard, M., Baines, D., Baker, S. G., Balaguer-Núñez, L., Balbinot, E., Balog, Z., Barache, C., Barbato, D., Barros, M., Barstow, M. A., Bartolomé, S., Bassilana, J. L., Bauchet, N., Baudesson-Stella, A., Becciani, U., Bellazzini, M., Bernet, M., Bertone, S., Bianchi, L., Blanco-Cuaresma, S., Boch, T., Bombrun, A., Bossini, D., Bouquillon, S., Bragaglia, A., Bramante, L., Breedt, E., Bressan, A., Brouillet, N., Bucciarelli, B., Burlacu, A., Busonero, D., Butkevich, A. G., Buzzi, R., Caffau, E., Cancelliere, R., Cánovas, H., Cantat-Gaudin, T., Carballo, R., Carlucci, T., Carnerero, M. I., Carrasco, J. M., Casamiquela, L., Castellani, M., Castro-Ginard, A., Castro Sampol, P., Chaoul, L., Charlot, P., Chemin, L., Chiavassa, A., Cioni, M. R. L., Comoretto, G., Cooper, W. J., Cornez, T., Cowell, S., Crifo, F., Crosta, M., Crowley, C., Dafonte, C., Dapergolas, A., David, M., David, P., de Laverny, P., De Luise, F., De March, R., De Ridder, J., de Souza, R., de Teodoro, P., de Torres, A., del Peloso, E. F., del Pozo, E., Delbo, M., Delgado, A., Delgado, H. E., Delisle, J. B., Di Matteo, P., Diakite, S., Diener, C., Distefano, E., Dolding, C., Eappachen, D., Edvardsson, B., Enke, H., Esquej, P., Fabre, C., Fabrizio, M., Faigler, S., Fedorets, G., Fernique, P., Fienga, A., Figueras, F., Fouron, C., Fragkoudi, F., Fraile, E., Franke, F., Gai, M., Garabato, D., Garcia-Gutierrez, A., García-Torres, M., Garofalo, A., Gavras, P., Gerlach, E., Geyer, R., Giacobbe, P., Gilmore, G., Girona, S., Giuffrida, G., Gomel, R., Gomez, A., Gonzalez-Santamaria, I., González-Vidal, J. J., Granvik, M., Gutiérrez-Sánchez, R., Guy, L. P., Hauser, M., Haywood, M., Helmi, A., Hidalgo, S. L., Hilger, T., Hładczuk, N., Hobbs, D., Holland, G., Huckle, H. E., Jasniewicz, G., Jonker, P. G., Juaristi Campillo, J., Julbe, F., Karbevska, L., Kervella,

P., Khanna, S., Kochoska, A., Kontizas, M., Kordopatis, G., Korn, A. J., Kostrzewa-Rutkowska, Z., Kruszyńska, K., Lambert, S., Lanza, A. F., Lasne, Y., Le Campion, J. F., Le Fustec, Y., Lebreton, Y., Lebzelter, T., Leccia, S., Leclerc, N., Lecoeur-Taibi, I., Liao, S., Licata, E., Lindstrøm, E. P., Lister, T. A., Livanou, E., Lobel, A., Madrero Pardo, P., Managau, S., Mann, R. G., Marchant, J. M., Marconi, M., Marcos Santos, M. M. S., Marinoni, S., Marocco, F., Marshall, D. J., Martin Polo, L., Martín-Fleitas, J. M., Masip, A., Massari, D., Mastrobuono-Battisti, A., Mazeh, T., McMillan, P. J., Messina, S., Michalik, D., Millar, N. R., Mints, A., Molina, D., Molinaro, R., Molnár, L., Montegriffo, P., Mor, R., Morbidelli, R., Morel, T., Morris, D., Mulone, A. F., Munoz, D., Muraveva, T., Murphy, C. P., Musella, I., Noval, L., Ordénovic, C., Orrù, G., Osinde, J., Pagani, C., Pagano, I., Palaversa, L., Palicio, P. A., Panahi, A., Pawlak, M., Peñalosa Esteller, X., Penttilä, A., Piersimoni, A. M., Pineau, F. X., Plachy, E., Plum, G., Poggio, E., Poretti, E., Poujoulet, E., Prša, A., Pulone, L., Racero, E., Ragaini, S., Rainer, M., Raiteri, C. M., Rambaux, N., Ramos, P., Ramos-Lerate, M., Re Fiorentin, P., Regibo, S., Reylé, C., Ripepi, V., Riva, A., Rixon, G., Robichon, N., Robin, C., Roelens, M., Rohrbasser, L., Romero-Gómez, M., Rowell, N., Royer, F., Rybicki, K. A., Sadowski, G., Sagristà Sellés, A., Sahlmann, J., Salgado, J., Salguero, E., Samaras, N., Sanchez Gimenez, V., Sanna, N., Santoveña, R., Sarasso, M., Schultheis, M., Sciacca, E., Segol, M., Segovia, J. C., Ségransan, D., Semeux, D., Shahaf, S., Siddiqui, H. I., Siebert, A., Siltala, L., Slezak, E., Smart, R. L., Solano, E., Solitro, F., Souami, D., Souchay, J., Spagna, A., Spoto, F., Steele, I. A., Steidelmüller, H., Stephenson, C. A., Süveges, M., Szabados, L., Szegedi-Elek, E., Taris, F., Tauran, G., Taylor, M. B., Teixeira, R., Thuillot, W., Tonello, N., Torra, F., Torra, J., Turon, C., Unger, N., Vaillant, M., van Dillen, E., Vanel, O., Vecchiato, A., Viala, Y., Vicente, D., Voutsinas, S., Weiler, M., Wevers, T., Wyrzykowski, Ł., Yoldas, A., Yvard, P., Zhao, H., Zorec, J., Zucker, S., Zurbach, C., & Zwitter, T. 2021, A&A, 649, A1

Gallet, F. & Bouvier, J. 2015, A&A, 577, A98

Gao, X. 2018, ApJ, 869, 9

García, R. A., Hekker, S., Stello, D., Gutiérrez-Soto, J., Handberg, R., Huber, D., Karoff, C., Uytterhoeven, K., Appourchaux, T., Chaplin, W. J., Elsworth, Y., Mathur, S., Ballot, J., Christensen-Dalsgaard, J., Gilliland, R. L., Houdek, G., Jenkins, J. M., Kjeldsen, H., McCauliff, S., Metcalfe, T., Middour, C. K., Molenda-Zakowicz, J., Monteiro, M. J. P. F. G., Smith, J. C., & Thompson, M. J. 2011, MNRAS, 414, L6

García, R. A., Mathur, S., Pires, S., Régulo, C., Bellamy, B., Pallé, P. L., Ballot, J., Barceló Forteza, S., Beck, P. G., Bedding, T. R., Ceillier, T., Roca Cortés, T., Salabert, D., & Stello, D. 2014, A&A, 568, A10

Gordon, T. A., Davenport, J. R. A., Angus, R., Foreman-Mackey, D., Agol, E., Covey, K. R., Agüeros, M. A., & Kipping, D. 2021, ApJ, 913, 70

Gould, A., Bahcall, J. N., & Flynn, C. 1996, ApJ, 465, 759

Hardegree-Ullman, K. K., Cushing, M. C., Muirhead, P. S., & Christiansen, J. L. 2019, AJ, 158, 75

Holmberg, J., Nordström, B., & Andersen, J. 2007, A&A, 475, 519

Howard, W. S., Corbett, H., Law, N. M., Ratzloff, J. K., Galliher, N., Glazier, A., Fors, O., del Ser, D., & Haislip, J. 2020, ApJ, 895, 140

Kado-Fong, E., Williams, P. K. G., Mann, A. W., Berger, E., Burgett, W. S., Chambers, K. C., Huber, M. E., Kaiser, N., Kudritzki, R. P., Magnier, E. A., Rest, A., Wainscoat, R. J., & Waters, C. 2016, ApJ, 833, 281

Kawaler, S. D. 1988, ApJ, 333, 236

Keppens, R., MacGregor, K. B., & Charbonneau, P. 1995, A&A, 294, 469

Krishnamurthi, A., Pinsonneault, M. H., Barnes, S., & Sofia, S. 1997, ApJ, 480, 303

Lanzafame, A. C. & Spada, F. 2015, A&A, 584, A30

Laughlin, G., Bodenheimer, P., & Adams, F. C. 1997, ApJ, 482, 420

Liu, F., Asplund, M., Yong, D., Meléndez, J., Ramírez, I., Karakas, A. I., Carlos, M., & Marino, A. F. 2016, MNRAS, 463, 696

Lomb, N. R. 1976, Ap&SS, 39, 447

Lu, Y. L., Angus, R., Curtis, J. L., David, T. J., & Kiman, R. 2021, AJ, 161, 189

MacGregor, K. B. & Brenner, M. 1991, ApJ, 376, 204

Magnier, E. A. & Cuillandre, J. C. 2004, PASP, 116, 449

Magnier, E. A., Schlafly, E. F., Finkbeiner, D. P., Tonry, J. L., Goldman, B., Röser, S., Schilbach, E., Casertano, S., Chambers, K. C., Flewelling, H. A., Huber, M. E., Price, P. A., Sweeney, W. E., Waters, C. Z., Denneau, L., Draper, P. W., Hodapp, K. W., Jedicke, R., Kaiser, N., Kudritzki, R. P., Metcalfe, N., Stubbs, C. W., & Wainscoat, R. J. 2020, ApJS, 251, 6

Mamajek, E. E. & Hillenbrand, L. A. 2008, ApJ, 687, 1264

Mann, A. W., Feiden, G. A., Gaidos, E., Boyajian, T., & von Braun, K. 2015, ApJ, 804, 64

Mathur, S., García, R. A., Bugnet, L., Santos, Â. R. G., Santiago, N., & Beck, P. G. 2019, Frontiers in Astronomy and Space Sciences, 6, 46

Mathur, S., Salabert, D., García, R. A., & Ceillier, T. 2014, Journal of Space Weather and Space Climate, 4, A15

Matt, S. P., Brun, A. S., Baraffe, I., Bouvier, J., & Chabrier, G. 2015, ApJ, 799, L23

McInnes, L., Healy, J., & Astels, S. 2017, Journal of Open Source Software, 2, 205

McQuillan, A., Aigrain, S., & Mazeh, T. 2013, MNRAS, 432, 1203

Meibom, S., Barnes, S. A., Platais, I., Gilliland, R. L., Latham, D. W., & Mathieu, R. D. 2015, Nature, 517, 589

Meibom, S., Mathieu, R. D., & Stassun, K. G. 2009, ApJ, 695, 679

Montgomery, K. A., Marschall, L. A., & Janes, K. A. 1993, AJ, 106, 181

Newton, E. R., Irwin, J., Charbonneau, D., Berlind, P., Calkins, M. L., & Mink, J. 2017, ApJ, 834, 85

Newton, E. R., Irwin, J., Charbonneau, D., Berta-Thompson, Z. K., Dittmann, J. A., & West, A. A. 2016, ApJ, 821, 93

Newton, E. R., Mondrik, N., Irwin, J., Winters, J. G., & Charbonneau, D. 2018, AJ, 156, 217

Nissen, P. E., Twarog, B. A., & Crawford, D. L. 1987, AJ, 93, 634

Önehag, A., Korn, A., Gustafsson, B., Stempels, E., & Vandenberg, D. A. 2011, A&A, 528, A85

Pace, G., Pasquini, L., & François, P. 2008, A&A, 489, 403

Pires, S., Mathur, S., García, R. A., Ballot, J., Stello, D., & Sato, K. 2015, A&A, 574, A18

Popinchalk, M., Faherty, J. K., Kiman, R., Gagné, J., Curtis, J. L., Angus, R., Cruz, K. L., & Rice, E. L. 2021, ApJ, 916, 77

Press, W. H. & Rybicki, G. B. 1989, ApJ, 338, 277

Rebull, L. M., Stauffer, J. R., Bouvier, J., Cody, A. M., Hillenbrand, L. A., Soderblom, D. R., Valenti, J., Barrado, D., Bouy, H., Ciardi, D., Pinsonneault, M., Stassun, K., Micela, G., Aigrain, S., Vrba, F., Somers, G., Christiansen, J., Gillen, E., & Collier Cameron, A. 2016, AJ, 152, 113

Rebull, L. M., Stauffer, J. R., Hillenbrand, L. A., Cody, A. M., Bouvier, J., Soderblom, D. R., Pinsonneault, M., & Hebb, L. 2017, ApJ, 839, 92

Reinhold, T., Bell, K. J., Kuszlewicz, J., Hekker, S., & Shapiro, A. I. 2019, A&A, 621, A21

Roquette, J., Matt, S. P., Winter, A. J., Amard, L., & Stasevic, S. 2021, MNRAS, 508, 3710

Salabert, D., García, R. A., Beck, P. G., Egeland, R., Pallé, P. L., Mathur, S., Metcalfe, T. S., do Nascimento, J. D., J., Ceillier, T., Andersen, M. F., & Triviño Hage, A. 2016, A&A, 596, A31

Salabert, D., García, R. A., Jiménez, A., Bertello, L., Corsaro, E., & Pallé, P. L. 2017, A&A, 608, A87

Sandquist, E. L., Mathieu, R. D., Quinn, S. N., Pollack, M. L., Latham, D. W., Brown, T. M., Esselstein, R., Aigrain, S., Parviainen, H., Vanderburg, A., Stello, D., Somers, G., Pinsonneault, M. H., Tayar, J., Orosz, J. A., Bedin, L. R., Libralato, M., Malavolta, L., & Nardiello, D. 2018, AJ, 155, 152

Santos, A. R. G., García, R. A., Mathur, S., Bugnet, L., van Saders, J. L., Metcalfe, T. S., Simonian, G. V. A., & Pinsonneault, M. H. 2019, ApJS, 244, 21

Santos, N. C., Lovis, C., Pace, G., Melendez, J., & Naef, D. 2009, A&A, 493, 309

Scargle, J. D. 1982, ApJ, 263, 835

Simonian, G. V. A., Pinsonneault, M. H., Terndrup, D. M., & van Saders, J. L. 2020, ApJ, 898, 76

Skumanich, A. 1972, ApJ, 171, 565

Somers, G. & Pinsonneault, M. H. 2016, ApJ, 829, 32

Somers, G., Stauffer, J., Rebull, L., Cody, A. M., & Pinsonneault, M. 2017, ApJ, 850, 134

Spada, F. & Lanzafame, A. C. 2020, A&A, 636, A76

Stassun, K. G., Oelkers, R. J., Paegert, M., Torres, G., Pepper, J., De Lee, N., Collins, K., Latham, D. W., Muirhead, P. S., Chittidi, J., Rojas-Ayala, B., Fleming, S. W., Rose,

M. E., Tenenbaum, P., Ting, E. B., Kane, S. R., Barclay, T., Bean, J. L., Brassuer, C. E., Charbonneau, D., Ge, J., Lissauer, J. J., Mann, A. W., McLean, B., Mullally, S., Narita, N., Plavchan, P., Ricker, G. R., Sasselov, D., Seager, S., Sharma, S., Shiao, B., Sozzetti, A., Stello, D., Vanderspek, R., Wallace, G., & Winn, J. N. 2019, AJ, 158, 138

Stello, D., Vanderburg, A., Casagrande, L., Gilliland, R., Silva Aguirre, V., Sandquist, E., Leiner, E., Mathieu, R., & Soderblom, D. R. 2016, ApJ, 832, 133

Stetson, P. B. 1987, PASP, 99, 191

Taylor, B. J. 2007, AJ, 133, 370

Tonry, J. L., Stubbs, C. W., Lykke, K. R., Doherty, P., Shivvers, I. S., Burgett, W. S., Chambers, K. C., Hodapp, K. W., Kaiser, N., Kudritzki, R. P., Magnier, E. A., Morgan, J. S., Price, P. A., & Wainscoat, R. J. 2012, ApJ, 750, 99

van Saders, J. L. & Pinsonneault, M. H. 2013, ApJ, 776, 67

van Saders, J. L., Pinsonneault, M. H., & Barbieri, M. 2019, ApJ, 872, 128

VandenBerg, D. A. & Stetson, P. B. 2004, PASP, 116, 997

VanderPlas, J. T. 2018, ApJS, 236, 16

Weber, E. J. & Davis, Leverett, J. 1967, ApJ, 148, 217

Winters, J. G., Henry, T. J., Jao, W.-C., Subasavage, J. P., Chatelain, J. P., Slatten, K., Riedel, A. R., Silverstein, M. L., & Payne, M. J. 2019, AJ, 157, 216

Wright, N. J., Drake, J. J., Mamajek, E. E., & Henry, G. W. 2011, ApJ, 743, 48

Zechmeister, M. & Kürster, M. 2009, A&A, 496, 577

# Chapter 3

# Temporal Tomography

## 3.1 Introduction

Adaptive optics (AO) instrumentation encompasses a wide range of systems that measure, and correct for, the loss in image quality that results from turbulence in the Earth's atmosphere. Early AO systems generally had a wavefront sensor (WFS) which measured the shape of the incoming wavefront, a real time controller (RTC) that computed the correction needed for a flat wavefront, and a deformable mirror (DM) that applied this correction to the light. These systems were designed around relatively few site characteristics. Distributions of values that described the turbulence strength (Fried parameter, $r_0$) and the speed at which it evolved (Greenwood time delay, $\tau_0$) were sufficient to set the system requirements and understand the expected performance. However, more complex AO systems require additional knowledge of a site's turbulence characteristics.

The vertical profile of the turbulence above a site is a key piece of additional knowledge needed for multi-conjugate AO (MCAO) or ground layer AO (GLAO) systems, where the goal is to push the AO correction to larger fields of view. There are a variety of techniques used to measure the turbulence profile. Combined Multi-Aperture Scintillation Sensor–Differential Image Motion Monitor (MASS-DIMM; Kornilov et al. 2007) units and SCIntillation Detection And Ranging (SCIDAR; Vernin & Roddier 1973; Rocca et al. 1974) are capable of providing accurate vertical profiles but require separate, dedicated

instrumentation. Alternative techniques like SLOpe Detection And Ranging (SLODAR; Wilson 2002) allow these measurements to be done using the data collected during the regular operation of systems with multiple WFSs, critical for developing a long term picture of turbulence characteristics. Other advanced AO systems, such as Extreme AO (ExAO) require detailed knowledge of the temporal characteristics of a site's turbulence. SLODAR and SCIDAR have been generalized to yield wind profiles in addition to the vertical turbulence profile aiding in this endeavor. Additionally, techniques such as Fourier Wind Identification (FWI; Poyneer et al. 2009) are able to extract wind data, though without any altitude information.

Here, we report our progress on an extension to FWI that we have been developing. The goal is to combine external measurements of the vertical wind profile with WFS data to: 1) identify turbulent layers in the atmosphere, 2) assign them an altitude based on their wind speed and direction, and 3) exploit their unique temporal characteristics to assist in tomographic AO control. In particular we consider the application of this technique to GLAO, where the goal is to filter out the free atmosphere signal in the WFS measurements and thus improve the estimate of the ground layer. We call this technique "temporal tomography." It is temporal in its reliance on the temporal power spectra of the WFS data and tomographic in that different layers in the atmosphere have distinct and identifiable velocities. Successful temporal tomography is expected to yield a number of benefits. By reducing the signal of the free atmosphere, fewer guide stars are required to obtain an accurate measure of the ground layer turbulence. This would reduce the cost of laser guide star-based systems by requiring fewer laser beacons and wavefront sensors. For natural guide star-based systems, requiring fewer stars of sufficient brightness in the field will increase the sky coverage of the system. Such benefits would facilitate the widespread adoption of GLAO.

## 3.2 Method

The basic principle behind temporal tomography is that atmospheric layers with different wind vectors will have power concentrated at different temporal frequencies. In theory, any modal basis for which this is true (e.g., Zernike modes Roddier et al. 1993) can be used with the concepts laid out in this section. Here, we use the complex Fourier modes of the slopes as our basis for their simple connection to the layer velocities under the assumption of frozen flow.

### 3.2.1 Complex Fourier Modes

The complex Fourier modal basis was originally developed as an extension of the real Fourier modal basis used in Optimized-gain Fourier Control (OFC; Poyneer & Véran 2005). The goal was to create a modal basis that was amenable to use with a predictive control algorithm for ExAO observations (Predictive Fourier Control or PFC; Poyneer et al. 2007). This basis assumes a square grid for the slopes or actuators on the DM, providing a $N \times N$ grid of Fourier modes. For a grid that is spatially indexed by $\langle x, y \rangle$ and a Fourier mode indexed by $\langle k, l \rangle$[1] the mode is defined by

$$F_{k,l}[x, y] = e^{j2\pi \frac{[kx+ly]}{N}}. \tag{3.1}$$

Computing the modal coefficients is then accomplished by taking the discrete Fourier transform (DFT) of the data, which can be accomplished using one of the many implementations of the fast Fourier transform (e.g., FFTW3)[2]. In both OFC and PFC the general approach is to compute the Fourier modal coefficients by a forward DFT applied to the slopes, apply various real or complex-valued filters to the slope Fourier modes including a

[1] In this dissertation, I take an approach to the indexing similar to that of `numpy` arrays, where negative indices index from the opposite end of the array. For example, $\langle k, l \rangle = \langle -2, -3 \rangle$ is equivalent to $\langle k, l \rangle = \langle N-2, N-3 \rangle$ for an $N \times N$ array.

[2] If you read this, then I owe you a drink of your choosing, feel free to to reach out to me about this.

"reconstruction filter" which converts the slope Fourier modes into actuator Fourier modes[3], and then apply an inverse DFT which converts the Fourier modes into actuator space. However, for our work we do not take the step of applying a reconstruction filter. Instead we have chosen to operate on the slope Fourier modes and transform back into a filtered set of wavefront sensor slopes, at which point the slopes are processed in the same manner as a standard matrix-based system. We did this to simplify our on-sky tests (Sec. 3.4) as our DM does not have a square layout for the actuators. Moreover, since it is a curvature DM the natural shapes are closer to the second derivative of the wavefront as opposed to the integrated phase that is common to most DM implementations.

A significant advantage of the complex Fourier modes over their real counterparts is their temporal behavior, particularly under frozen flow conditions. As an illustrative example, let us consider the example of a singular Fourier mode phase aberration translating across the aperture of the telescope. The phase evolves with time as

$$\phi\left(x,y,t\right)=\cos\left(\frac{2\pi}{Nd}\left[k(x-v_xt)+l(y-v_yt)\right]\right) \tag{3.2}$$

where $\langle k,l\rangle$ is the 2D spatial frequency of the Fourier mode, $\langle v_x,v_y\rangle$ is the velocity vector, and $d$ is the subaperture size. By rearranging the argument of the cosine function to spell out the phase term

$$\phi\left(x,y,t\right)=\cos\left(\frac{2\pi}{Nd}(kx+ly)-\frac{2\pi}{Nd}(kv_x+lv_y)t\right) \tag{3.3}$$

it becomes straightforward to write out the modal coefficient by accounting for the fact that the DFT output for a function $A\cos(\vec{\omega}\cdot\vec{x}-\xi)$ is simply $\frac{A}{2}e^{j\xi}$. The modal coefficient for this phase aberration is then

$$\Phi_{k,l}(t)=\frac{1}{2}e^{j2\pi\frac{\left[kv_x+lv_y\right]}{Nd}t} \tag{3.4}$$

[3]There are a couple subtleties to keep in mind when doing phase reconstruction by this method, since we skip this step in our work details on these can be found in Appendix 3.6.1.

which evolves with a single temporal frequency

$$f_t = -\frac{(kv_x + lv_y)}{Nd} \tag{3.5}$$

The sign of $f_t$ can be positive or negative, depending on how the wind vector projects onto the frequency vector of that Fourier mode (i.e., the sign of the dot product of the two vectors). Critically, in this description a single frozen turbulent layer will contribute to the modal coefficient only at the temporal frequency $f_t$.

In reality a Fourier mode of a frozen, turbulent layer in the atmosphere will not evolve quite as cleanly since new unmeasured turbulence is blowing into the optical path of the telescope. Fortunately, for frozen flow the Fourier modes are nearly uncorrelated both temporally and spatially (Poyneer et al. 2007). Because of this we can approximate the temporal evolution of the Fourier mode as a random process driven by temporally white noise, such as a first order autoregressive model. The Fourier mode then evolves as

$$\Phi_{k,l}[t] = \alpha\Phi_{k,l}[t-1] + w[t], \tag{3.6}$$

where $\alpha$ is a complex number with magnitude less than 1 and $w[t]$ is temporally white noise. The magnitude of $\alpha$ encodes the degree to which the layer is frozen, with values closer to 1 indicating turbulence that is more frozen. The argument encodes the temporal frequency of the layer, and thus the wind vector of the layer, and can be expressed as

$$\arg(\alpha) = -2\pi\frac{f_t}{f_s}, \tag{3.7}$$

where $f_s$ is the sampling rate of the WFS. The temporal PSD of a Fourier mode described by this model still exhibits the majority of its power concentrated around the frequency $f_t$. Though as alpha decreases the less concentrated this power becomes (i.e., the PSD of the layer begins to broaden, spreading the power across more temporal frequencies).

However, the atmosphere is not always guaranteed to exhibit frozen flow. Regardless, the model of Eq. 3.6 can still be a sufficient description of how the Fourier mode evolves in time. In a first order autoregressive model the magnitude of alpha can be thought of as a measure of the influence the previous timestep $(t-1)$ has on the current timestep $(t)$. Small values for the magnitude of alpha lead to less influence, hence the broadening of the power spectrum. Thus, non-frozen turbulence can be modeled using autoregressive models with smaller values of alpha. Critically, this is not strictly a property of the atmosphere alone. The phase of alpha is dependent on the sampling rate of the WFS; therefore two systems observing in the same conditions will experience different values for alpha, with the faster system observing a value of alpha closer to one (and thus, observing a more frozen atmosphere).

### 3.2.2 Temporal Tomogragphy

Since atmospheric layers with different wind vectors will have different characteristic frequencies ($f_t$ values) one can, in principle, temporally filter the data to remove the signal associated with individual layers. With external measurements, models, or predictions of the vertical wind profile one can select these layers on the basis of altitude, aiding in tomographic reconstruction. This filtering can be achieved in real time with the use of digital filters applied to the observed modes in the RTC. Because the WFS data is regularly sampled in time there is a wealth of existing design techniques and implementations that can be leveraged to accomplish this task.

Digital filters can be sorted into two categories, recursive (or infinite impulse response; IIR) filters and nonrecursive (or finite impulse response; FIR) filters. The primary advantage of IIR filters over their FIR counterparts is the efficiency in implementation, requiring fewer calculations for a filter of similar design (e.g., the same low pass filter implemented as IIR versus FIR). This comes at the cost of more complex design as well as a non-linear phase response. However, we use low order filters of common types (e.g., low pass and bandstop) meaning the design of these filters are well understood with various existing prescriptions

(e.g., Butterworth or Chebyshev Type 1 filters). Because of these existing prescriptions, as well as the more efficient computation, we have focused this discussion on IIR filter design. Future work should include detailed study of the impact of a non-linear phase response on the phase reconstruction.

The canonical equation describing the output of a recursive filter at a timestep $t$ is

$$b_0 y[t] = a_0 x[t] + a_1 x[t-1] + ... + a_n x[t-n] - b_1 y[t-1] - ... - b_m y[t-m]. \quad (3.8)$$

Where $x$ is the unfiltered input (e.g., the Fourier mode coefficient prior to any filtering), $y$ is the filtered version of the input, and $a_i$ and $b_i$ are the recursion coefficients whose values determine the behavior of the filter, with $b_0$ generally being set to 1. For example, a first order low pass filter can be implemented as

$$a_0 = 1 - x; b_1 = x; x = e^{-2\pi f_c} \quad (3.9)$$

where $f_c$ is the cutoff frequency and is a value normalized by the sample rate of the system, thus it is between 0 and 0.5 (i.e., the maximum cutoff frequency is the Nyquist frequency).

The transfer function is a convenient representation for both understanding the response of a filter, as well as how to design one. It is related to Eq. 3.8 by the Z-transform, which converts discrete time signals into the complex frequency domain. The transfer function for an IIR filter of Eq. 3.8 is

$$H(z) = \frac{\sum_{i=0}^{n} a_i z^{-i}}{\sum_{j=0}^{m} b_j z^{-j}} \quad (3.10)$$

where, after dividing out the leading coefficient $a_0$, we can factor the numerator and denominator giving

$$H(z) = g \frac{\prod_{i=1}^{n}(1 - q_i z^{-1})}{\prod_{j=0}^{m}(1 - p_j z^{-1})}. \quad (3.11)$$

In this form the $g$ is called the gain of the filter, the $q_i$ values are the "zeros", and the $p_i$ values are the "poles". The zeros are where the filter attenuates the signal, and the poles are where the filter boosts the signal. Both $q_i$ and $p_i$ are complex numbers, and their magnitude

determines the strength of the attenuation/boost, whereas the argument determines the frequency on which the effect is centered. Designing a filter is then a balancing act of placing zeros and poles in the right places in the complex plane to give the desired filter response as a function of frequency.

Traditionally, the signal that is being filtered is strictly real valued (e.g., a signal consisting of voltages in a circuit) therefore poles and zeros are chosen in pairs that are complex conjugates. For example, consider the simple case of a filter with a single zero at 30 Hz for a system with a sampling frequency of 200 Hz. In this case, the zero is $e^{j2\pi\frac{30\text{ Hz}}{200\text{ Hz}}}$ which yields the recursion coefficients $a_0 = 0.5$, $a_1 = -0.2939 - 0.4045j$. If we add a second zero at -30 Hz, $e^{-j2\pi\frac{30\text{ Hz}}{200\text{ Hz}}}$, then the recursion coefficients become $a_0 = 0.3149$, $a_1 = -0.3702$, $a_2 = 0.3149$. Since the power spectrum of real values is symmetric about 0 Hz this filter behaves identically to the single zero version, but now with the added benefit of not producing complex output for real input.

However, for the Fourier modes that we seek to filter in temporal tomography the input is complex, and this was chosen specifically for the fact that the positive and negative frequencies encode additional information about the wind direction. Because of this, our filter design must take care to ensure that the poles and zeros are not paired with their complex conjugates, ensuring that our recursion coefficients will be complex-valued. This means that the standard prescriptions for computing recursion coefficients had to be modified slightly for bandstop filters. As an example, consider the design of a Butterworth bandstop filter for -30 Hz with a 10 Hz bandwidth using the tools available in any standard signal processing toolbox (e.g., `MATLAB` or `scipy.signal`). First, one generates the standard set of recursion coefficients for a 30 Hz bandstop with 10 Hz bandwidth, then converts these to zeros and poles form. Calculate the argument for each pole/zero and remove the ones with the opposite sign as where the filter is intended to be centered, for this example any pole/zero with a positive argument. Finally, convert the new set of poles and zeros back to recursion coefficient form.

This modification to the standard filter design is sufficient to create filters which are asymmetric about 0 Hz. However, they are still limited to the other standard assumptions that are included in the prescriptions. In particular is the assumption that a filter is intended to entirely reject the power at the specified frequencies, at least the level of many decibels of attenuation. This is not always the desired outcome for temporal tomography. The power spectra of individual atmospheric layers can be quite broad, and thus the ground layer may contribute a non-negligible fraction of the power at the $f_t$ value of a free atmosphere layer. In this case, a blanket rejection of all the power at $f_t$ will make the estimate of the ground layer worse. Ultimately, a new prescription of filter design is needed that accounts for variable filter depth, achievable through tuning of the magnitude of the zeros. This development will be critical future work for the development of successful temporal tomography.

## 3.3 Feasibility

### 3.3.1 Atmospheric Statistics

Critical to our approach is that the wind vectors are different enough to be resolved as separate peaks in the power spectra of the Fourier modes. To understand how frequently this is the case for separating the ground layer turbulence from the free atmosphere we compared the velocities of ground layer and free atmosphere winds using the vertical profiles of wind speeds and directions from the Maunakea Weather Center's data archive. For the free atmosphere wind speeds and directions we use the profiles provided by the Global Forecasting System (GFS) weather models[4]. The GFS models for Maunakea provide a forecasted wind speed and direction for 13 different layers in the atmosphere, at pressures ranging from 700 millibars to 100 millibars, in steps of 50. Every six hours a new forecast is produced which includes the predicted wind speed and direction for each layer at times ranging from 0 hours to 180 hours into the future. Every 12 hours the model is updated to include data collected from weather balloons launched from the Hilo International Airport,

[4]The archival data can be found on this page of the website.

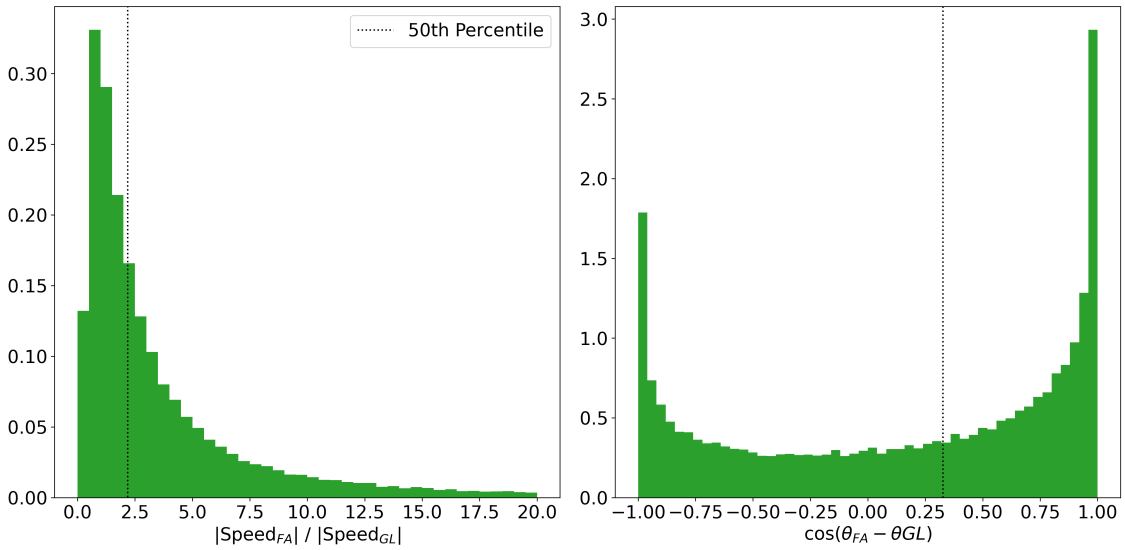


Figure 3.1: **Left Panel**: The distribution of the ratios of the free atmosphere wind speed to the ground layer wind speed. **Right Panel**: The distribution of the dot product of the unit vectors of the free atmosphere and ground layer wind directions. **Both Panels**: The full distributions of the metrics discussed in Sec. 3.3.1, computed for 1551 nights spanning January 1st, 2018 to July 6th, 2022. The vertical dotted line is the 50th percentile. By these two metrics the ground layer is easily separable from the free atmosphere based on wind vectors $\sim 67\%$ of time.

and thus the 0-hour forecasts from the GFS models at 00:00 and 12:00 (UTC) accurately represent the measured vertical profile of the wind. We restricted our dataset to the nighttime profiles, giving us one profile per night, from January 1st, 2018 to July 6th, 2022. Finally, the pressure at the summit is typically close to 600 millibars, so we only considered the layers with pressures of 550 millibars or less to be free atmosphere, which yielded 10 free atmosphere layers per night.

For the ground layer wind speeds and directions we use the CFHT weather tower[5]. Because these data are reported every 5 minutes, whereas the free atmosphere values are only available once a night, we computed a nightly mean and standard deviation from the CFHT measurements to serve as representative values. The mean ground layer wind vector is calculated component-wise and the standard deviation of the speeds is calculated using the standard method applied to the measured wind speeds. The standard deviation of the directions is estimated using the Yamartino methodYamartino (1984), which properly accounts for the fact that angles are periodic. Specifically, for $n$ measurements of the wind direction $\theta$:

$$\sigma_\theta = \arcsin(\epsilon)\left[1 + \left(\frac{2}{\sqrt{3}} - 1\right)\epsilon^3\right] \tag{3.12}$$

where $\epsilon = \sqrt{1 - (s_a^2 + c_a^2)}$, $s_a = \frac{1}{n}\Sigma_i^n \sin\theta_i$, and $c_a = \frac{1}{n}\Sigma_i^n \cos\theta_i$. We then characterized each night with three ground layer wind speeds/directions, the mean and the mean plus or minus one standard deviation.

Next, we considered two metrics for how different the ground layer wind was from the free atmosphere layers in a given night. First, we calculated the ratio of the wind speeds: $\frac{\text{Speed}_{FA}}{\text{Speed}_{GL}}$, since the wind speed is directly proportional to the $f_t$-value of the layer this value corresponds roughly to the ratio of the free atmosphere $f_t$ to the ground layer $f_t$, the farther this value is from one, the better. Second, we calculated the dot product of the unit direction vectors: $\cos(\theta_{FA} - \theta_{GL})$. These values ranged from -1 to 1, and again the farther this value

[5]The archival data can be found on this page of the website.

is from one, the better. Then for each night we calculated these values for every combination of 3 ground layer speed/directions and 10 free atmosphere speed/directions, giving 30 wind speed ratios and 30 wind direction dot products per night. The full distribution of each of these metrics can be seen in Fig. 3.1.

Ultimately, the ability to resolve two separate peaks in the power spectrum will also depend on the AO system that is being used and the characteristics of the turbulence itself. Nonetheless, these distributions provide useful, if rough, estimates for how often temporal tomography can be expected to successfully sort atmospheric layers between ground layer and free atmosphere. A best case scenario is when the ground layer and the free atmosphere layer have directions that are anti-aligned (i.e. $\cos(\theta_{FA} - \theta_{GL}) < 0$), as this means the $f_t$ value for each layers will always have opposite signs. For all the nights in our sample, this is the case $\sim$ 36% of time. Of the nights where the two are roughly aligned (i.e. $\cos(\theta_{FA} - \theta_{GL}) > 0$), then they must have different speeds for temporal tomography to work. If we conservatively require the two layers to be different by a factor of two (i.e. $\frac{\text{Speed}_{FA}}{\text{Speed}_{GL}} > 2$ or $\frac{\text{Speed}_{FA}}{\text{Speed}_{GL}} < 0.5$), this covers another $\sim$ 31% of all nights. This means that for $\sim$ 67% of all the nights on Maunakea over the past five years the ground layer is easily separable from the free atmosphere layers based on wind speed and direction alone.

### 3.3.2 Simulations

To further demonstrate the feasibility of temporal tomography in GLAO systems we have run simulations of a handful of illustrative cases. In each case we simulated an open loop GLAO system consisting of 1, 2, 3, or 5 natural guide stars. We used the University of Hawaii 88" telescope (UH88") aperture, 2.2 m in diameter with a 40% central obscuration. The WFSs were Shack-Hartmann-like with $8 \times 8$ subapertures and a frame rate of 200 Hz, in line with the 'imaka GLAO demonstrator on the UH88" telescope (Chun et al. 2016). They are Shack-Hartmann-like in that the slopes were calculated as a direct average of the gradient of the phase screen in a subaperture, with no additional noise. Guide stars were spaced equally along a circle of diameter 15' except in the 1 guide star case, which was

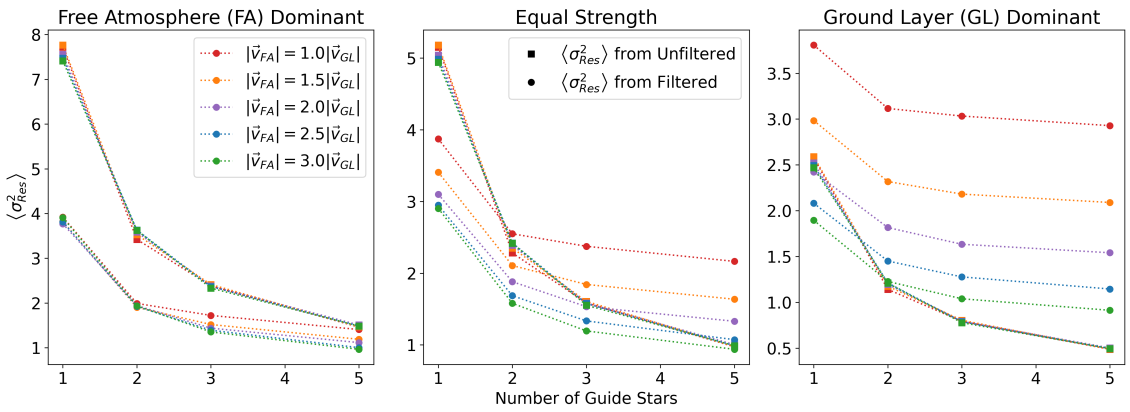


Figure 3.2: The mean variance of the residual wavefronts for each simulation, where the residual wavefront is the difference between an estimation of the ground layer and the ideal reconstruction of the ground layer. In each panel the color corresponds to the wind speed of the free atmosphere for that simulation, squares represent the results of the standard GLAO reconstruction and circles represent the reconstruction with filtering of the slope Fourier modes. When the atmosphere is dominated by the free atmosphere filtering allows a 2 guide star system to perform comparably to a 5 guide star system. On a ground layer dominant night the filter that was used removes some of the ground layer signal as well, resulting in a worse estimate than the standard approach.

on-axis. The atmosphere was a two-layer atmosphere, one layer at a height of 0 m (the ground layer) and one at 2 km (the free atmosphere). Phase screens are evolved following the approach of (Assémat et al. 2006). Finally, for each case we also simulated a second one-layer atmosphere that was composed of an identical ground-layer with no free atmosphere.

The simulated cases consisted of three night types: 1) a ground layer dominant night, where the ground layer contributes $\frac{3}{4}$ of the total phase variance, 2) an equal strength night, where the two layers contribute equally, and 3) free atmosphere dominant night, where the free atmosphere contributes $\frac{3}{4}$ of the total phase variance. For each of these night types we also varied the free atmosphere wind speed, from 1 to 3 times (in half steps) faster than ground layer wind speed of 6.5 m/s. In all cases the ground layer moves to the North, while the free atmosphere moves to the East. These directions are chosen as a compromise between the ideal case (anti-aligned wind vectors) and the worst case (aligned wind vectors). Conditions on Maunakea generally favor the free atmosphere and ground layer being anti-aligned or orthogonal in direction (see Sec. 3.3.1 for details).

For each simulated case open loop slopes were recorded for 8192 steps. At each step we did three different reconstructions using the Southwell geometry (Southwell 1980). The first is the standard estimate of the ground layer, which takes the reconstructed wavefront from each available guide star and averages them together. The second is the temporal tomography version. In this case we applied a notch reject recursive filter to the slopes' complex Fourier modes, the bandwidth was a fixed 15 Hz and the central frequency for each mode was set by $f_t$ given by Eq. 3.5, plugging in the known free atmosphere wind vector. After filtering the Fourier modes for each guide star we applied the inverse DFT, reconstructed the wavefronts, and averaged them together. The third case is from the simulations where only the ground layer is present. Because they had no free atmosphere included it represented the best possible reconstruction of the ground layer. The residual wavefront from the difference between one of our estimates and this idealized measure is the amount of free atmosphere turbulence included in that estimate. We calculated the variance of the residual wavefronts for both estimates at every time step in each simulation, and then took the mean of each series of 8192 variances. These mean variances are plotted in Fig. 3.2, the smaller these variances are the better, with a value of 0 meaning the system matched the perfect case exactly.

In general we see that as the number of guide stars increases, the overall benefit of temporal tomography decreases, this is expected as you are averaging over more realizations of the free atmosphere turbulence. On nights when the free atmosphere is dominant, temporal tomography helps 2 and 3 guide star systems substantially, offering performance that is comparable to having 5 guide stars in the standard approach. On nights where the layers are of equal strength, 2 and 3 guide star systems benefit—though not as strongly as when the free atmosphere dominates. For ground layer dominant nights and equal strength nights with 5 guide star systems the filtered slopes actually produce a worse estimate of the ground layer than doing nothing at all. This is because the power of atmospheric layers is only strongest at $f_t$, they still contribute power at other temporal frequencies. Therefore, the deep notch reject filter used here is also filtering out the ground layer's contribution at

$f_t$. As conditions shift towards ground layer dominated conditions the relative contributions to the total power at $f_t$ shift as well requiring less aggressive filtering to remove the free atmosphere contribution. Finally, we see that the faster the free atmosphere wind speed is the more effective temporal tomography is, which is simply a statement that the larger the difference in $f_t$ values between two layers, the easier it is to treat them separately.

We find these results highly encouraging, especially given the clear avenues we have for improving the performance of temporal tomography in all conditions. In particular they highlight the need for improved filter design, as the ideal temporal tomography system will provide no benefit at all in the worst case scenarios. However, this result does also highlight a limitation of the current simulations, as the atmospheric model used produces temporal power spectra that are much broader than what has been observed on-sky. Therefore, a critical avenue for future work will be developing turbulence simulations with more realistic temporal characteristics. An added benefit would be the ability to simulate non-frozen turbulence, important for simulating temporal tomography in slower AO systems.

## 3.4 On-sky Tests

Table 3.1: Parameters of our observations for the on-sky tests of temporal tomography.

| Parameter | Value |
|---|---|
| Start Date | 2022, September 7 (UTC) |
| End Date | 2022, September 12 (UTC) |
| Field Center | 19:33:44.8, +07h49'46" |
| Filter Used | Johnson I |
| WFS 0 Location | +0.4', +5.3' away from the center |
| WFS 1 Location | +6.5', -2.6' away from the center |
| WFS 2 Location | -8.1', -3.4' away from the center |
| WFS 3 Location | +0.0', +0.0' away from the center |

During an observing run from September 7th, 2022 to September 12, 2022 we ran a set of on-sky experiments using the 'Imaka GLAO demonstrator on the UH88" telescope. The target was a crowded field of stars in the galactic plane centered on RA: 293.4367,

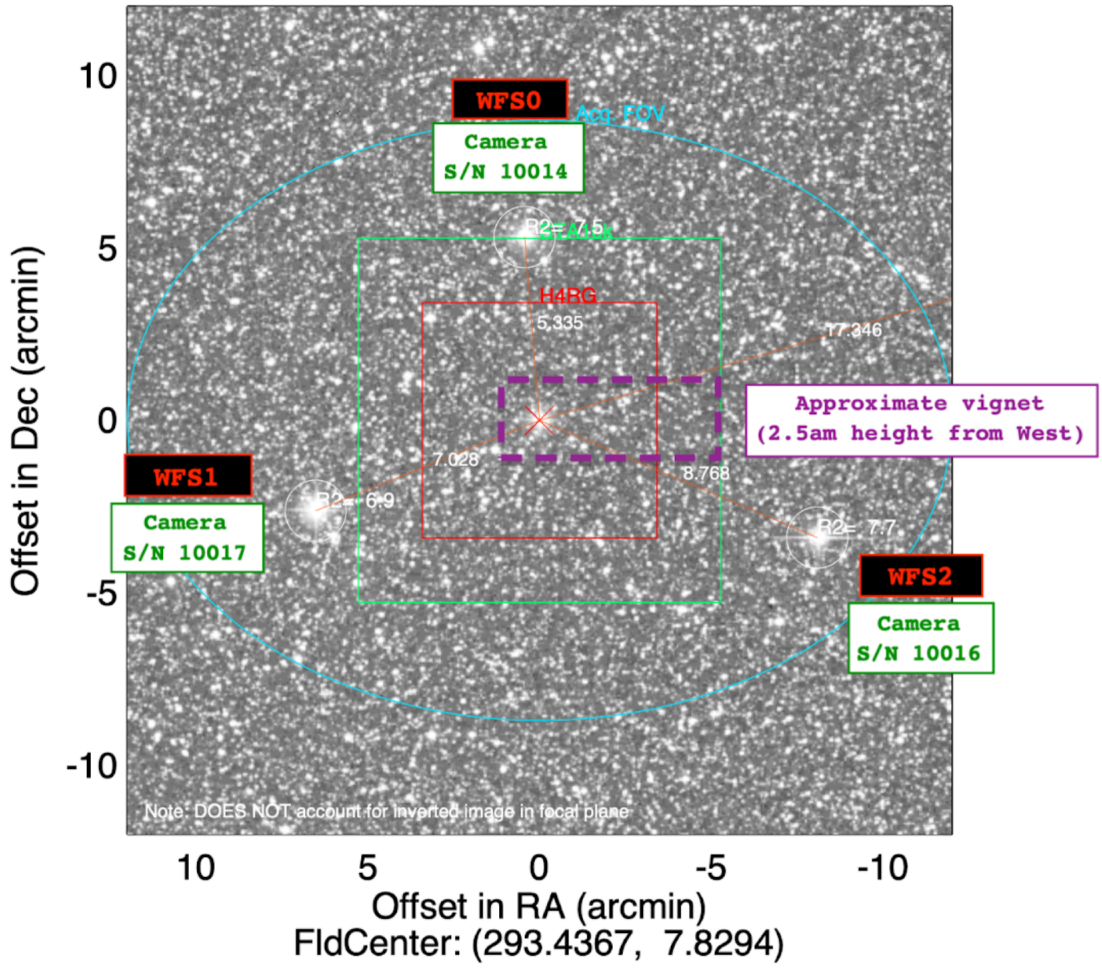


Figure 3.3: The finder chart and instrument configuration for our observations of Fld2. The camera used for this particular observing run was STAcam, with the field of view denoted by the green square.

Table 3.2: A summary of the observing modes from our on-sky tests.

| Date (UT) | # of GS | Filter Parameters | # of Images |
|---|---|---|---|
| September 8, 2022 | 4 | Low Pass at 40 applied to pseudo-open loop (POL) slopes | 1 |
| | 4 | Low Pass at 40 applied to closed loop slopes | 1 |
| | 4 | Low Pass at 60 applied to POL slopes | 11 |
| | 4 | Low Pass at 60 applied to closed loop slopes | 10 |
| September 9, 2022 | 4 | Low Pass at 30 applied to POL slopes | 3 |
| | 3 | Low Pass at 30 applied to POL slopes | 1 |
| | 2 | Low Pass at 30 applied to POL slopes | 1 |
| | 1 | Low Pass at 30 applied to POL slopes | 1 |
| | 4 | Low Pass at 40 applied to POL slopes | 6 |
| | 4 | Low Pass at 50 applied to POL slopes | 2 |
| | 4 | Low Pass at 60 applied to POL slopes | 10 |
| | 3 | Low Pass at 60 applied to POL slopes | 1 |
| | 2 | Low Pass at 60 applied to POL slopes | 1 |
| | 1 | Low Pass at 60 applied to POL slopes | 1 |
| September 10, 2022 | 4,3,2,1 | Asymm. Low Pass for wind  18 knots and 45° | 4 |
| | 4,3,2,1 | Bandstop for wind at 18 m/s and 34° 10 Hz bandwidth | 1 |
| | 4,3,2,1 | Bandstop for wind at 22 m/s and 34° 12 Hz bandwidth | 1 |
| | 4,3,2,1 | Bandstop for wind at 20 m/s and 34° 12 Hz bandwidth | 9 |
| September 11, 2022 | 4,3,2,1 | Bandstop for wind at 23 m/s and 50° 8 Hz bandwidth | 2 |
| | 4,3,2,1 | Bandstop for wind at 25 m/s and 45° 12 Hz bandwidth | 1 |
| | 4,3,2,1 | Bandstop for wind at 25 m/s and 45° 15 Hz bandwidth | 3 |
| | 4,3,2,1 | Bandstop for wind at 22 m/s and 34° 15 Hz bandwidth | 1 |
| September 12, 2022 | 4,3,2,1 | Asymm. Low Pass for wind at 25.5 m/s and 225° | 5 |
| | 4,3,2,1 | Bandstop for wind at 25.5 m/s and 225° 20 Hz bandwidth | 2 |

Dec: 7.8294 which we refer to as "Fld2" (Fig. 3.3). For the run 'Imaka was configured to use four natural guide stars, the details of which are listed in Table 3.1. The specifics of the experiment varied from night to night, with the details of what was tested each night summarized in Table 3.2.

Prior to the run we updated the 'Imaka RTC to include the option of running the system in a temporal tomography mode. In order to simplify our modifications to the code we decided to include the temporal tomography as an extra step that was inserted in between the standard steps of computing the WFS centroids and performing the reconstruction. In this way the temporal tomography could be easily turned on and off without needing to modify the control loop, allowing us to quickly cycle between observing modes. This minimized the effect of changing atmospheric conditions in between images.

The modifications to the control system itself were relatively simple, with memory allocated for storing the past few sets of Fourier modes that had been calculated (both filtered and unfiltered, as needed for recursive filtering), and a set of recursion coefficients for each mode. When running with temporal tomography the RTC would 1) calculate the centroids from the WFS data, 2) calculate the FFT of the centroids, 3) compute a filtered version of each Fourier mode coefficient using the recursion coefficients as well as the past few Fourier mode coefficients (both filtered and unfiltered), 4) apply the inverse FFT to the now filtered Fourier mode coefficients producing a set of filtered centroids, and 5) use the filtered centroids to compute the next DM command. Since each Fourier mode has a different $f_t$ value that needs to be filtered, we elected to write external python code to handle generating arrays of recursion coefficients. This code took an input wind vector, calculated the $f_t$ for each Fourier mode, and then generated a set of recursion coefficients for each $f_t$ value. Because our filter design was limited to filters with near 100% attenuation at the central frequencies we also included a minimum frequency cutoff. Any $f_t$ value below the frequency cutoff was left unfiltered in order to preserve the performance of the system at low temporal frequencies, where the ground layer turbulence and dome seeing are generally expected to be (less than 10-20 Hz). Finally, because the $f_t$ value for tip and tilt

($\langle k, l \rangle = \langle 0, 0 \rangle$) is 0 Hz irrespective of the wind vector, this mode is left unfiltered and thus passed on to the reconstruction unaltered (i.e., the system corrects all the tip/tilt that it sees, even if it originates from the free atmosphere).

Two versions of the filtering were implemented in advance of the run. First was the pseudo-open loop version, where pseudo-open loop slopes were reconstructed from the WFS slopes and the current voltages applied to the DM. These slopes were then put through the filtering process before being converted back to closed loop form by subtracting out the slope offsets that were added to convert to pseudo-open loop slopes. The second mode was to simply apply the filtering process to the closed loop slopes. Comparisons between the two modes indicate they do not behave any differently, in line with our expectations.

While the observations were ordered in an effort to minimize differences in the seeing variations, the conditions during this particular run were rather poor, severely limiting our ability to draw any significant conclusions from the data collected (Fig. **??**). The seeing varied significantly even between images that were adjacent in the observing sequence. Importantly, the simulations suggested that incorrect filtering could significantly reduce the accuracy of the ground layer estimate. However, the filtering does not appear to harm our results. This is a potential sign that the temporal power of atmospheric layers is more concentrated than expected from our simulations, indicating favorable conditions for temporal tomography. As for whether or not our observations benefited from the use of temporal tomography is inconclusive for now, many more data points spanning a wider range of observing conditions will be required. Fortunately, there are plans to continue testing this into the future.

## 3.5 Conclusion

We have introduced the concept of temporal tomography and laid out the work that has been done in developing this idea. In particular we have framed this development in terms of aiding the tomography of GLAO systems which enable high resolution wide-field

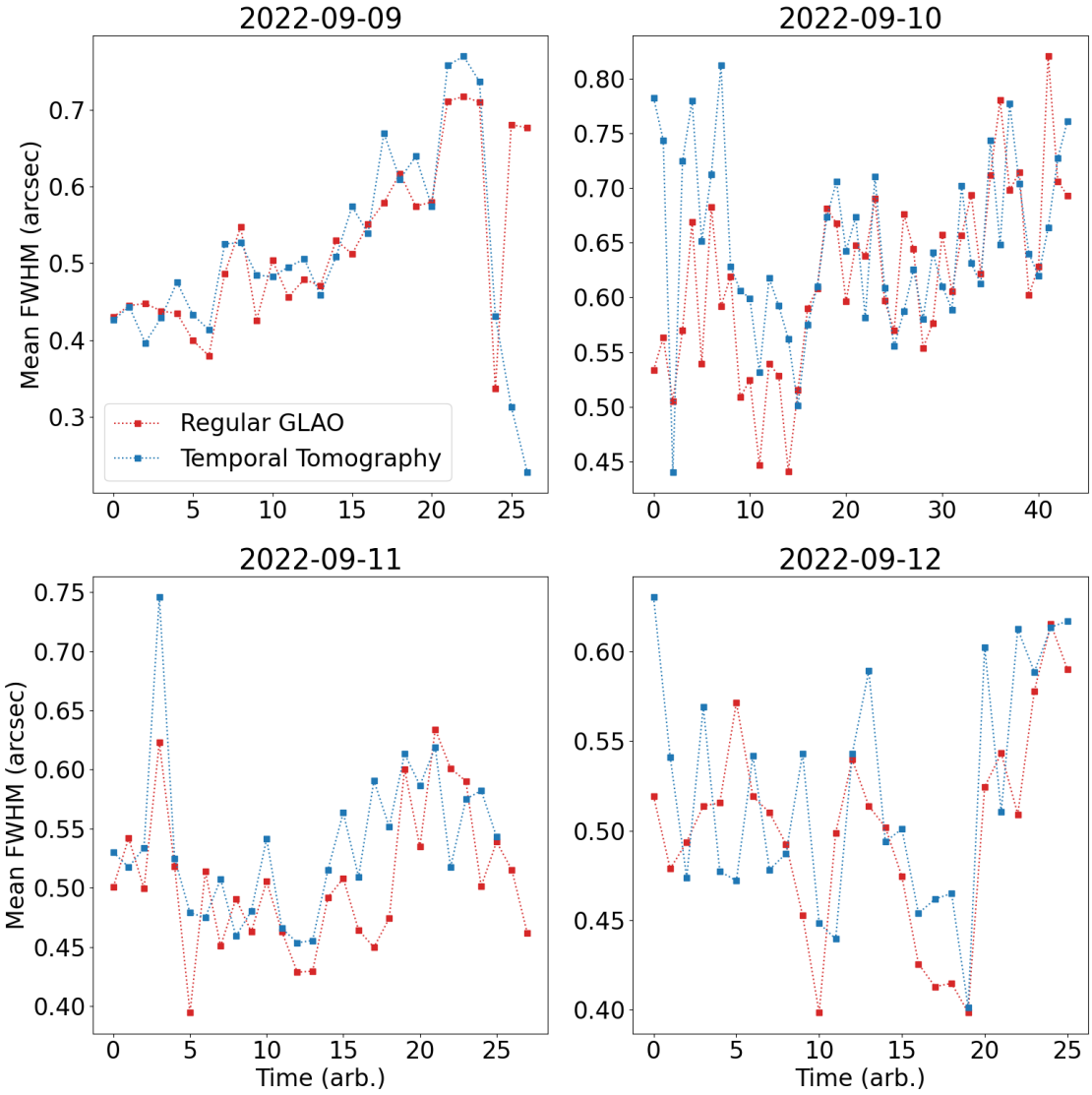


Figure 3.4: The results of our on-sky tests during the September observing run with ʻImaka. Each panel is one of the selected nights, in blue is the mean FWHM of the image for an image taken while running temporal tomography. In red is an image taken without running temporal tomography. Points that are aligned vertically represent pairs, where both have an identical configuration other than whether or not temporal tomography was used. Because of our observing strategy, these images were taken adjacent in time (i.e., they are separated by no more than 5 minutes).

imaging. Using meteorological data dating back to January 1st, 2018 we have demonstrated that conditions on Maunakea are typically favorable for the use of temporal tomography. With simulations we showed that even a naive implementation of the temporal tomography approach is expected to yield improved estimates of the ground layer turbulence, though this does depend on the atmospheric conditions. Finally, we have summarized the results of our first on-sky tests in which we used temporal tomography during actual GLAO observations, though the results remain inconclusive for the time being.

The work summarized in this chapter has laid the groundwork for a great deal of future research in aiding tomographic AO systems of all varieties. Critical future research will include continuing on-sky work to test the system in a wider range of atmospheric conditions. Particularly challenging will be interpreting these results, as on-sky conditions can vary rapidly and the difference between with and without temporal tomography is likely to be at a level comparable to these changing conditions. Developing the right metrics both for measuring variation across the field as well as a "seeing normalized" mean point spread function for comparisons across time will be necessary for making a strong case for temporal tomography. Furthermore, development of a formalized mathematical framework for recursive filters with arbitrary attenuation will be needed for ensuring temporal tomography can function in any conditions, and this will require more detailed simulation work. Analysis of datasets for other important astronomical sites will broaden the applicability of temporal tomography and help in the goal of bringing GLAO systems to many more telescopes across the globe.

## 3.6 Appendix

### 3.6.1 Fourier Transform Reconstruction

When taking the extra step of calculating the phase Fourier modes from the slope Fourier modes the behavior of the edge apertures becomes critical to achieving an accurate reconstruction. After several iterations on the proper technique Poyneer & Véran (2005)

settled on a technique they refer to as "edge correction". Prior to computing the slope Fourier modes they modify the two x slopes just outside the aperture in each row and the two y slopes just outside the aperture in each column of subapetures. These values are each set to minus one times the sum of that row or column. This approach yields a phase that is flat outside the aperture. After applying the edge correction and then the DFT to the WFS slopes the phase Fourier modes can be computed using a filter such as the modified-Hudgin filter for an $N \times N$ system

$$\hat{P}[k,l] = \frac{e^{-j\pi\frac{l}{N}}\left[e^{-j2\pi\frac{k}{N}} - 1\right]X[k,l] + e^{-j\pi\frac{k}{N}}\left[e^{-j2\pi\frac{l}{N}} - 1\right]Y[k,l]}{4\left[\sin^2\left(\frac{\pi k}{N}\right) + \sin^2\left(\frac{\pi l}{N}\right)\right]}. \tag{3.13}$$

Where X and Y are the x and y slope Fourier modes, respectively. Importantly the piston mode $\langle k,l\rangle = \langle 0,0\rangle$ is set to zero to prevent division by zero.

### 3.6.2 The Hermitian Symmetry of the Complex Fourier Modes

When the input to a DFT is strictly real then the output will have Hermitian symmetry, for two dimensional data that means most modes will come in pairs carrying redundant information (e.g., $\langle k,l\rangle$ and $\langle -k,-l\rangle$ are complex conjugates). As a result there are only $\frac{N^2}{2} - 2$ unique complex Fourier modes for an $N \times N$ system. Regardless, a filter must be applied to every one of the $N^2$ modes before applying the inverse DFT to obtain the filtered slopes. In order to ensure that the filtered slopes are real values, the Hermitian symmetry of the complex Fourier modes must be preserved. Thankfully, this can be accomplished through the use of filters which are complex conjugates of each other. For example, say the atmospheric layer that needs to be filtered has an $f_t$ value of 30 Hz in the mode $\langle 2,3\rangle$, the simplest filter places the zero at $e^{j2\pi\frac{30\text{ Hz}}{200\text{ Hz}}}$ yielding the recursion coefficients $a_0 = 0.5$, $a_1 = -0.2939 - 0.4045j$. Then the filter that must be applied to the mode $\langle -2,-3\rangle$ will be one with a zero of $e^{-j2\pi\frac{30\text{ Hz}}{200\text{ Hz}}}$ which in turn has the recursion coefficients $a_0 = 0.5$, $a_1 = -0.2939 + 0.4045j$. In doing this, the Fourier coefficients of $\langle 2,3\rangle$ and $\langle -2,-3\rangle$ remain complex conjugates, preserving the Hermitian symmetry of the complex Fourier modes.

Without this, the output of the DFT that computes the filtered slopes will be complex, and thus incompatible with phase reconstruction.

### 3.6.3 Aliasing in the WFS Slopes

Spatial aliasing is a concern for any control system using the complex Fourier modes. The ideal solution is to use a spatially filtered WFS which prevents the aliasing of higher order modes from occurring in the first place. However, even without a spatially filtered WFS the use of Fourier modes is still feasible. Higher order modes that have been aliased into the WFS slopes can produce additional peaks in the temporal PSDs at $f_t$ values that lack analytical descriptions. However, our simulations indicate that they contain only a small fraction of the total power. Our on-sky observations show no such peaks suggesting they are below the noise floor of our data, consistent with the predictions from our observations.

# References


Assémat, F., Wilson, R., & Gendron, E. 2006, Optics Express, 14, 988

Chun, M. R., Lai, O., Toomey, D., Lu, J. R., Service, M., Baranec, C., Thibault, S., Brousseau, D., Hayano, Y., Oya, S., Santi, S., Kingery, C., Loss, K., Gardiner, J., & Steele, B. 2016, in Society of Photo-Optical Instrumentation Engineers (SPIE) Conference Series, Vol. 9909, Adaptive Optics Systems V, ed. E. Marchetti, L. M. Close, & J.-P. Véran, 990902

Kornilov, V., Tokovinin, A., Shatsky, N., Voziakova, O., Potanin, S., & Safonov, B. 2007, MNRAS, 382, 1268

Poyneer, L., van Dam, M., & Véran, J.-P. 2009, Journal of the Optical Society of America A, 26, 833

Poyneer, L. A., Macintosh, B. A., & Véran, J.-P. 2007, Journal of the Optical Society of America A, 24, 2645

Poyneer, L. A. & Véran, J.-P. 2005, Journal of the Optical Society of America A, 22, 1515

Rocca, A., Roddier, F., & Vernin, J. 1974, Journal of the Optical Society of America (1917-1983), 64, 1000

Roddier, F., Northcott, M. J., Graves, J. E., McKenna, D. L., & Roddier, D. 1993, Journal of the Optical Society of America A, 10, 957

Southwell, W. H. 1980, Journal of the Optical Society of America (1917-1983), 7, 998

Vernin, J. & Roddier, F. 1973, Journal of the Optical Society of America (1917-1983), 63, 270

Wilson, R. W. 2002, MNRAS, 337, 103

Yamartino, R. J. 1984, Journal of Applied Meteorology and Climatology, 23, 1362

# Chapter 4

# Conclusions

In this dissertation I have provided a new catalog of 1807 members of the open cluster M67 based on Gaia EDR3 parallaxes and proper motions. Using r and i photometry from Pan-STARRS1 DR2 I identified potential unresolved binaries and derived effective temperatures of all the candidate low mass members. For these stars we found 294 rotation periods, which were used to produce a sample of 4 Gyr old late K and early M dwarfs for use in calibrating gyrochonological or stellar spin-down models. To aid in this, I also provided a polynomial fit to this data as a function of effective temperature or the r-i color. Using these results I showed that solid body spin-down is the most likely candidate for describing stellar spin-down between the ages of 2.7 and 4 Gyr. This, combined with the long rotation periods of stars approaching the fully convective boundary make a compelling case for the core-envelope decoupling theory. Indeed, I showed that the core-envelope decoupling model was among the best, and is the only model launched from the zero age main sequence to provide a reasonable agreement with our observations of M67.

However, the book is not closed on M dwarf gyrochronology and the case for core-envelope decoupling, while compelling, is not complete. Future work is needed to cover a wider range of masses, particularly including M dwarfs which are fully convective. During the work on this dissertation observations of the cluster Ruprecht 147 (2.7 Gyr old) were completed, and will be reduced using the pipeline developed for this work. These observations will greatly increase the coverage of calibrators for M dwarf gyrochronology,

and are expected to include stars which are fully convective. At time of writing there are also on-going observations of NGC 752 (1.4 Gyr old) that will also probe stars through the fully convective boundary. Together these two clusters will provide much needed data on when the M dwarfs converge onto the slow rotator sequence. Critically, they will help to pin down the age at which M dwarfs fully converge onto a slow rotator sequence, something that is needed for accurate gyrochronology.

I have also introduced the concept of temporal tomography and laid out the work that has been done in developing this idea. In this dissertation the focus of this development was on assisting the tomographic reconstruction in GLAO systems, as a means of improving high resolution wide-field imaging applications. I used meteorological data and simulations to demonstrate the overall feasibility of the approach, even when using a fairly simple implementation of the technique. The results were very promising, though testing it on-sky has thus far proved quite challenging. There is a great deal of work still to be done in developing this approach, but the critical groundwork has been completed. Continuing on-sky tests to provide results in a wider range of conditions, as well as developing more precise tests for improvements yielded by temporal tomography are important future work that I will be carrying out. Additionally, I will be deriving a set of equations that allow one to compute the $a/b$ coefficients of a recursive filter given input parameters of central frequency, bandwidth, and filter depth. Finally, bringing temporal tomography to other tomographic AO systems is an important avenue of future work. I am very excited to see how this idea continues to develop, and am particularly hopeful that it will result in the creation of cheaper GLAO systems enabling even smaller observatories to use GLAO in regular operations.